DESIGN OF FUNCTIONALLY GRADED COMPLIANT MECHANISMS USING TOPOLOGY OPTIMIZATION

BY

CIAN CONLAN-SMITH

THESIS

Submitted in partial fulfillment of the requirements
for the degree of Master of Science in Aerospace Engineering
in the Graduate College of the
University of Illinois at Urbana-Champaign, 2017

Urbana, Illinois

Advisor:

Professor Kai A. James

Abstract

This research applies topology optimization to create feasible functionally graded complaint mechanism designs with the aim of improving structural performance compared to traditional homogeneous compliant mechanism designs. Structural performance is assessed with respect to mechanical/geometric advantage and stress distributions. A novel modified solid isotropic material with penalization (SIMP) method is adopted for representing local element material properties in FGM structures. The method of moving asymptotes (MMA) is used in conjunction with adjoint sensitivity analysis to find the optimal distribution of material properties. Functionally graded materials (FGMs) have material properties that vary based on spatial position. Here, FGMs are implemented using two different resource constraints – one on the mechanism's volume and the other on the integral of the Young's modulus distribution throughout the design domain. Two sets of results are presented – polymeric and metallic designs. Geometric non-linear analysis based on the Neo-Hookean model for hyperelastic materials is used to solve the mechanics problem for polymeric designs, whereas analysis of metallic materials is solved using conventional linear finite element analysis (FEA). Tensile tests are performed to obtain the material properties used in the analysis. To ensure an accurate representation when using linear FEA, metallic designs are subject to stress constraints. A novel method of stress-based design for FGM structures is presented where local yield strength is a function of local Young's modulus. Results suggest that FGMs can achieve the desired improvements in structural performance for certain designs and can also have a favorable effect on the von Mises stress distribution.

Acknowledgments

Firstly, I would like to thank my advisor, Kai James, for all your support and guidance during my MSc. study. Your knowledge and professional expertise has been invaluable throughout this time, which has been a key factor in achieving my goals. You have also encouraged me to develop my skills within research, inspired me to continue this development in my future, and given me an enthusiasm for this area of research, all for which I am extremely grateful.

I would also like to thank my friend and colleague, Anurag Bhattacharyya, for always being there to talk through the problems that arise throughout my work. Not only am I grateful for your advice but also for the countless coffee breaks, chess games, and tennis matches when it was necessary to spend some time away from the office.

To my parents, Paula and Clive, and girlfriend, Maria, each of you has always believed in me, encouraged me to pursue my ambitions, and supported me whenever I needed you. I am truly lucky to have all of you. Thank you.

Table of Contents

List of Tables

List of Figures

List of Abbreviations

ASTM	American Society for Testing and Materials
DOF	Degree(s) of freedom
FEA	Finite element analysis
FGM	Functionally graded material(s)
GPa	Gigapascals
KKT	Karush-Kuhn-Tucker (condition)
min	Minute
mm	Millimeters
MMA	Method of moving asymptotes
MPa	Megapascals
N	Newtons
RHS	Right-hand side
SD	Strength-differential
SIMP	Solid isotropic material with penalization
UTM	Universal testing machine
VM	von Mises stress

List of Symbols

A_Ω	Area of the design domain
A_e	Area of element e
$\mathbf{B}$	Cauchy-Green left deformation tensor
$\bar{\mathbf{B}}$	Strain displacement matrix
C	Compliance
C_{min}	Minimum value of compliance (lower bound)
C_{max}	Maximum value of compliance (upper bound)
$\mathbf{C}$	Cauchy-Green right deformation tensor
d	Distance between element centroids
$\frac{d\square}{d\square}$	Implicit derivative operator
$\frac{\partial\square}{\partial\square}$	Explicit derivative operator
$\mathbf{D}$	Constitutive matrix
$\bar{\mathbf{D}}$	Constitutive matrix in terms of Lamé constants
e	Element index number
E_e	Effective Young's modulus of element e
E_l	Lower limit of Young's modulus
E_{min}	Minimum value of Young's modulus
E_u	Upper limit of Young's modulus
E_{tol}	Material boundary Young's modulus tolerance
E_0	Young's modulus of a material (non-penalized)
$\mathbf{f}$	Force vector, containing all nodal forces
$\mathbf{f}_{ext}$	Vector containing all nodal external forces
$\mathbf{f}_{int}$	Vector containing all nodal internal forces
$\mathbf{f}_{int,e}$	Vector containing nodal internal forces of element e
$\mathbf{f}_p$	Decomposed force vector corresponding to prescribed degrees of freedom

$\mathbf{f}_0$	Applied force location vector
F	An arbitrary function
$\bar{F}$	Bound of the function F
F_{in}	Input force
F_{out}	Output force
$\mathbf{F}$	Deformation gradient
g	Objective function
i	Iteration index number
$\mathbf{I}$	Identity matrix
J	Determinant of deformation gradient
$\mathbf{k}_e$	Local (or element) stiffness matrix for element e
$\mathbf{k}_0$	Unpenalized Local (or element) stiffness matrix
$\mathbf{K}$	Global stiffness matrix
$\mathbf{k}_{tan,e}$	Local tangent stiffness matrix
$\mathbf{K}_{tan}$	Global tangent stiffness matrix
$\mathbf{K}_{ff}$	Decomposed (tangent) stiffness matrix corresponding to free-free DOF's
$\mathbf{K}_{fp}$	Decomposed (tangent) stiffness matrix corresponding to free-prescribed DOF's
$\mathbf{K}_{pf}$	Decomposed (tangent) stiffness matrix corresponding to prescribed-free DOF's
$\mathbf{K}_{pp}$	Decomposed (tangent) stiffness matrix corresponding to prescribed-prescribed DOF's
M	Resource value
M_0	Maximum resource value
$\bar{M}$	Bound of resource fraction
N_e	Number of elements
N_r	Number of element centroids within filter radius
$\mathbf{N}$	Shape functions
p	Penalization parameter
r	Filter radius
$\mathbf{R}$	Global residual vector
$\mathbf{R}_f$	Decomposed residual vector corresponding to free DOF's
$\mathbf{R}_p$	Decomposed residual vector corresponding to prescribed DOF's
S	Stress constraint function
$\mathbf{S}$	Second Piola-Kirchoff stress
t	Thickness

$\square^T$	Transpose matrix operator
tr($\square$)	Trace matrix operator
$\mathbf{u}$	Displacement field vector containing all nodal displacements
$\mathbf{u}_e$	Vector containing nodal displacements of element e
$\mathbf{u}_f$	Decomposed displacement field corresponding to free DOF's
$\mathbf{u}_p$	Decomposed displacement field corresponding to prescribed DOF's
u_{in}	Input displacement
u_{out}	Output displacement
w_{ij}	Entry at ith row and jth column in the density filter matrix
$\bar{w_{ij}}$	Unnormalized filter weight
$\boldsymbol{W}$	Density filter matrix
$\mathbf{x}$	Vector of deformed element coordinates
$\mathbf{X}$	Vector of undeformed element coordinates
x	Independent design variable
$\boldsymbol{x}$	Vector containing all independent design variables
$\tilde{\boldsymbol{x}}$	Vector containing all physical design variables
x_e	Design variable of the element e
x_0	Volume fraction design variable
$x_{0,e}$	Volume fraction design variable of element e
$\boldsymbol{x}_0$	Vector containing all volume fraction design variables
x_1	Mixing ratio design variable
$x_{1,e}$	Mixing ratio design variable of element e
$\boldsymbol{x}_1$	Vector containing all mixing ratio design variables
x_{min}	Minimum material density value
x_{max}	Maximum material density value
x_{tol}	Material boundary density tolerance
$\Delta\mathbf{u}$	Change in displacement field
Δu_p	Change in displacement at location of applied force
$\Delta\theta$	Change in magnitude of applied force
ε	Correction factor in stress constraint
ε_x	Transverse strain in x-direction
ε_y	Transverse strain in y-direction
ε_z	Axial strain in z-direction

$\boldsymbol{\varepsilon}$	Local strain
ζ	Exponential in p-norm function
η	Stress constraint relaxation exponential
θ	Magnitude of applied force
$\boldsymbol{\lambda}$	Lagrangian multiplier
$\boldsymbol{\lambda}_e$	Decomposed Lagrangian multiplier corresponding to the DOF's of element e
$\boldsymbol{\lambda}_f$	Decomposed Lagrangian multiplier corresponding to free DOF's
$\boldsymbol{\lambda}_p$	Decomposed Lagrangian multiplier corresponding to prescribed DOF's
λ_0, μ_0	Lamé constants
λ_e, μ_e	Effective Lamé constants of element e
ν	Poison's ratio
Π_F	Arbitrary function, F, represented in augmented Lagrangian form
Π_g	Mechanical/Geometric advantage function in augmented Lagrangian form
Π_C	Compliance function in augmented Lagrangian form
Π_S	Stress constraint function in augmented Lagrangian form
$\boldsymbol{\sigma}$	Stress or Cauchy Stress
$\bar{\boldsymbol{\sigma}}$	Cauchy Stress in Voigt notation
σ_{VM}	von Mises stress
σ_y	Yield stress
$\sigma_{y,\bar{E}}$	Yield stress evaluated at $\bar{E}$
ϕ	Power law interpolation function
Φ	Potential energy
Ω	Design domain or global design space
Ω_e	Element domain or local design space
$\square^{-1}$	Inverse matrix operator
$\otimes$	Matrix outer product operator
$\int_A \square \, dA$	Integral operator over a defined domain, A
$\sum_a^b \square$	Sum operator between bounds a and b

Chapter 1

Introduction

1.1 An Introduction to Compliant Mechanisms

The main purpose of mechanisms is to transform an input motion, force, or energy at one location to an output at separate location. However, their most significant advantage is their ability to produce an output force or displacement which is higher than the input. This phenomenon is called mechanical (increasing force) or geometric (increasing displacement) advantage. Energy is conserved across the mechanism (excluding frictional losses) but if the output displacement is smaller than input displacement, the force at output must be greater than the input force to satisfy this conservation, or vice versa for geometric advantage. Traditionally this is achieved through the use of rigid-link mechanisms which incorporate rigid links connected at movable joints. Compliant mechanisms, however, transfer energy through the elastic deflection of structural members and the use of compliant joints. A comparison between these mechanisms is shown in Figure 1.1, represented by 4-bar linkages. Compliant mechanisms are light weight; require no lubrication; have a built-in restoring force due to their elastic nature; and experience less wear, friction and backlash compared to rigid link mechanisms. The methodology of using topology optimization for compliant mechanism design was first proposed by Sigmund [1] in 1997.

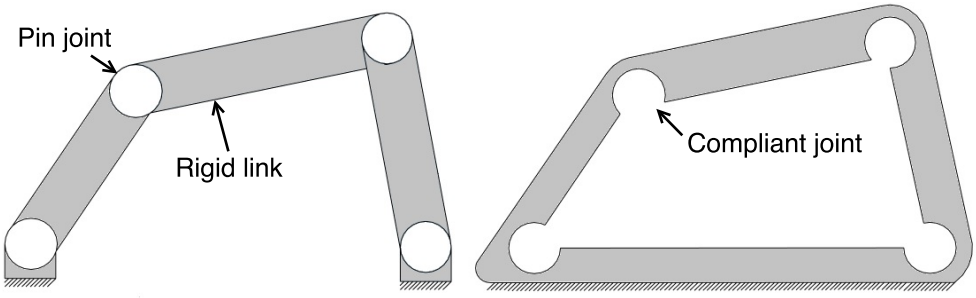

Figure 1.1: A traditional mechanism with rigid links and movable pin joints (left), and a compliant mechanism with compliant joints (right).

1.2 Motivation

In recent years compliant mechanisms have frequently been proposed for aerospace systems due to their advantages over traditional rigid-link mechanisms. As compliant mechanisms can be manufactured using fewer parts (usually one single part) they are lighter than their traditional counterparts. They are also easy to manufacture with modern 3D printing techniques, and do not require assembly. These advantages can have a large significance especially with the recent developments towards 3D printing in space [2, 3]. The ability to 3D print mechanisms and tools on board the International Space Station (or future bases on the Moon and Mars) will save substantially on the cost and time involved in transporting these devices from Earth. However, to achieve a broad-range of movement it is often necessary for compliant joints to be very thin. These thin members lead to increased localized stresses (stress concentrations), which cause limitations on the application of these mechanisms.

The motivation of this research is to seek more efficient compliant mechanism designs that can withstand higher load applications. We look to nature to solve this problem, more specifically to the human body. Throughout our body we have joints consisting of stiff bones, which act as structural members; and a combination of cartilage and synovial fluid between bones, which are compliant materials and allow movement. The joint mechanism receives power inputs from muscles and is held together by tendons (muscle to bone) and ligaments (muscle to muscle) [4]. Bones themselves consist of a graded type of material where their properties can vary depending on the position within the bone [5]. This wide range of different materials and material properties has been developed through millions of years of evolution to give us efficient joints throughout our body which act as mechanisms.

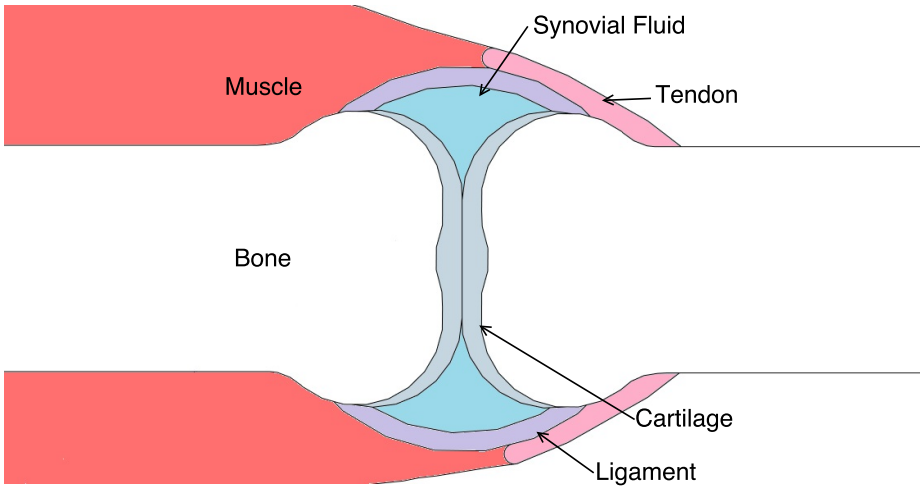

Figure 1.2: Schematic of a human joint detailing different materials.

This combination of stiff and compliant materials allows extensive motion at our joints while also allowing high load transmissions. The assumption is that by varying the material properties in compliant mechanisms, optimized solutions will concentrate a rubber-like compliant material at the joints while still using stiffer material for structural members, similar to the human joint. We hypothesize that by implementing heterogeneous materials, thus expanding the design space, improved geometric and mechanical advantages can be achieved, and thin structural members will be eliminated from the designs, improving stress distributions.

1.3 Functionally Graded Materials

One method for achieving these designs is through implementing multiple discrete materials. However, when using multiple materials there is a distinct boundary between any two materials which can produce a stress concentration across the interface [6]. In contrast, functionally graded materials (FGMs) can produce a gradual change in material properties, such as Young's Modulus, as a function of spatial position. This graded structure is achieved through a continuous change in composition and microstructure with respect to location [7]. FGMs can be represented by mixing two materials with some distinctly different material property.

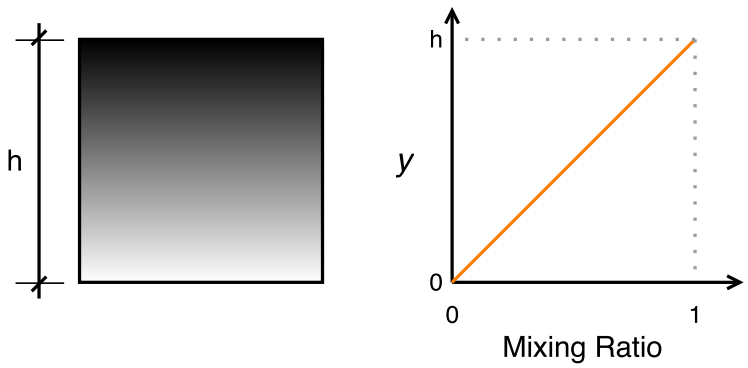

Figure 1.3: Heterogeneous material with gradation in y direction (left), and linear relationship between mixing ratio and position in the structure (right) i.e. a linear gradation of the material properties.

To date there has been little precedent in the literature for implementing FGMs compliant mechanism design with the purpose of improving structural performance. However there has been significant work on multiple material compliant mechanisms to achieve this goal. Alonso et al. [8] used a sequential element rejection and admission (SERA) method to produce 2- and 3-material compliant mechanism designs. This procedure considers separate material models (one for each material in the design) in which elements can be rejected or admitted from the material models via separate criteria. Yin and Anathasuresh [9] also produced multi-material compliant mechanism designs using a peak function method. Bendsøe and Sigmund introduced a solid isotropic material with penalization (SIMP) method for multiple material topology optimization [10]. Subsequently Sigmund has produced other SIMP based formulations for multi-material compliant mechanism design [11, 12]. Similar SIMP based formulations were also adopted by Stegmann and Lund [13] where each element is assigned two design variables – one for topology optimization and another for material optimization. Gaynor and coauthors produced and prototyped 2-material compliant mechanism designs through PolyJet 3D printing [14]. Here, 2 different SIMP based methods were used to produce optimized designs which were prototyped and tested experimentally for comparison.

There are some examples in the literature where FGMs are used in compliant mechanism design for different purposes. Carbonari et al. [15, 16] have modeled a functionally graded blend of piezoelectric and non-piezoelectric materials to produce actuators. These actuators have optimal topology and piezoelectric material distribution to produce an optimal overall performance. Similarly, Yin and Anathasuresh produced heterogeneous electro-thermal actuated compliant mechanisms consisting of blends of up to 3 materials using SIMP-based formulations [17]. There also examples of simultaneously optimizing topology and material gradation for structural applications. Xia [18] produced FGM beam structures using a level set method and interpreting any given point in the structure as a mixing ratio of two materials with differing modulus of elasticity. Stump et al. [19], introduced a method to design FGM distributions

with a tailored von Mises stress field.

1.4 Objectives

We hypothesize that FGMs will produce more efficient mechanisms with respect to mechanical/geometric advantage and stress distributions when compared to traditional homogeneous mechanisms. The objective of this work is to explore this hypothesis by studying the effect of mechanical results when incorporating FGMs into compliant mechanism design. Both polymeric and metallic mechanisms will be studied for this purpose. In order to model FGMs for topology optimization design it is required to develop methods for representing local element material properties within the structure. This work also aims to prototype designs and where possible, validate computational results experimentally.

1.5 Thesis Layout

Topology optimization is introduced in Chapter 2. This chapter will give a brief history of topology optimization, introduce basic definitions of optimization problems, review different methods of topology optimization, and provide more detailed descriptions of the basic methods adopted for this work. Chapter 3 signifies the progression into the more specific methods adopted for this work. This chapter will cover the mechanical analysis used to solve the various optimization problems presented in this thesis. Chapter 4 details the optimization methods used including problem definitions and sensitivity analysis. Chapter 5 will present all the results and discussion of findings, followed by a summary and concluding remarks in Chapter 6.

Chapter 2

Topology Optimization

The goal of structural optimization is to produce structural designs with optimal material layouts, sizing and shape. The concept of structural optimization was first published in 1904 by Australian inventor, Anthony Mitchel [20]. At the time this contribution had little impact and the contribution was not seen as significant until years later with the development of computers. In 1972 Rozvany extended this theory to optimal layout, or topologies, of beam structures [21, 22]. Sizing [23] and shape [24] optimization was introduced soon after. Sizing denotes the optimal thickness distribution or the optimal member cross-sectional areas in a truss structure for maximizing or minimizing the objective physical quantity while satisfying other design variables. Shape optimization has a similar objective but finds the optimal shape of the structure by varying the material domain boundary within a specified design domain. In 1988 Bendsøe and Kikuchi introduced an homogenization method for topology optimization [25]. This method treated topology optimization as a material distribution problem capable of producing optimal topologies, shapes, and sizes of structural members simultaneously. This chapter will focus on the methods adopted for topology optimization as a material distribution problem.

2.1 Topology Optimization as a Material Distribution Problem

Typically in this type of problem the methods follow a basic procedure similar to that outlined in Figure 2.1. Firstly a design domain is defined with inputs, boundary conditions and desired outputs (when necessary). An objective function is defined to maximize or minimize a physical quantity such as stiffness, compliance, mechanical advantage etc. The design domain is discretized into a number of cells (or elements) and an initial guess (initial condition) is set for the material distribution. Finite element analysis is then conducted on the current structure followed by sensitivity analysis of element material density values. In the optimization phase, sensitivity results are used to determine how each independent element density should vary to move towards an optimal distribution. The algorithm tests for convergence with the updated material distribution given specific user defined convergence criteria. If the design does not converged for the updated distribution, FEA is conducted on the new structure creating an iterative

procedure until the convergence criteria is satisfied. The converged result is an optimal solution to the design problem.

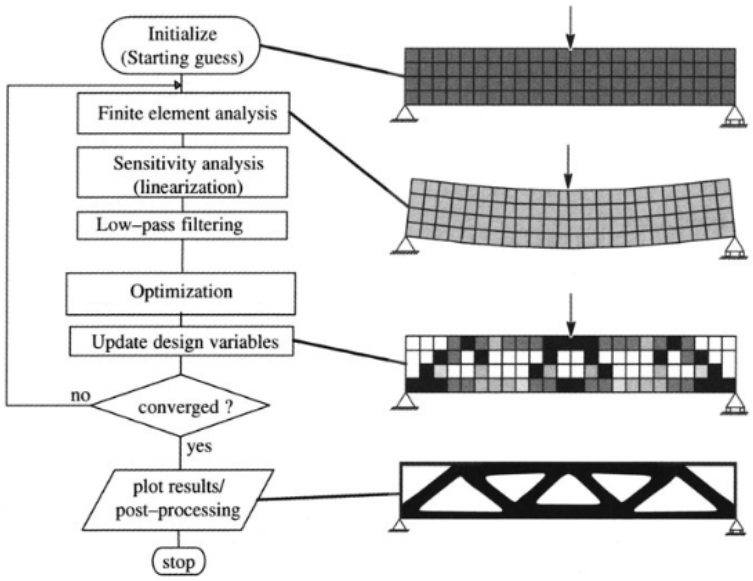

Figure 2.1: Generic stages of a Topology Optimization Problem [26]

The design domain represents a fixed region in physical space in which material is distributed to produce the most optimal structure. Optimality of the structure is defined by the objective function, g. Using numerical optimization techniques, material is distributed within the domain in order to minimize the value of g. This objective function is also subjected to any number of constraints. All topology optimization problems require at least one constraint to prevent the problem from being ill-posed. For example, in a compliance minimization (maximize stiffness) problem the objective function can always be decreased by adding more material to the design domain, therefore a volume constraint is required. Topology optimization problems are defined in the following manor

$$\begin{aligned} \min_{x} \quad &: \quad g(\mathbf{u}(\boldsymbol{x}),\mathbf{f}(\boldsymbol{x}),\boldsymbol{x}) \\ \text{subject to} \quad &: \quad F(\mathbf{u}(\boldsymbol{x}),\mathbf{f}(\boldsymbol{x}),\boldsymbol{x}) - \bar{F} \leq 0 \end{aligned} \tag{2.1}$$

where $\boldsymbol{x}$ are the design variables, the displacement vector, $\mathbf{u}$, and force vector, $\mathbf{f}$, are solutions to the mechanical analysis, F is the function used to calculate the value of the constraint, and $\bar{F}$ is the bound of the constraint. Note that the problem may be subject to multiple constraints, all of which take the same as in Eqn. 2.1.

2.2 SIMP Method

As mentioned previously, Bendsøe and Kikuchi developed the homogenization method [25], the first method of treating topology optimization as a material distribution problem. As previously discussed, a domain is defined and discretized into a series of cells. For this method, each cell contains a rectangular hole or a series of distributed rectangular holes. Homogenization theory is used to obtain a set of material properties for each cell while the cell's hole size is varied in order to gain an optimal solution. Cells with small holes are interpreted as solid material whereas cells with large holes are interpreted as void regions. Hole dimensions (width and height) in each cell and the orientation of the cell structure are regarded as design variables, which produces a large number of variables and decreases computational efficiency. The homogenization method was also the first topology optimization method capable of achieving optimal designs of both shape and sizing of members. The cell structure of the analysis introduced a fixed mesh which gave this method a significant advantage over other topology methods presented at the time.

The Solid Isotropic Material Penalization (SIMP) method takes a simplified form of the homogenization method. Like the homogenization method the specified design domain is meshed into a fixed grid and material is redistributed throughout the domain to find an optimal solution to maximize/minimize a specific objective function. Unlike the homogenization method which uses a microscale structure to introduce material density, the SIMP method incorporates material density as a non-physical independent variable. The SIMP method assumes that material properties are constant within each element. This eliminates the need to evaluate and determine microstructures and their orientation, thus reducing the number of variables from 3 to 1, and resulting in a higher computational efficiency. Sigmund et al. has provided a number of freely available topology optimization short MATLAB codes that exemplify the computation efficiency of the SIMP method [27, 28].

The SIMP method is often referred to as the power law approach. The effective material stiffness for a given element, E_e, is expressed as the product of the materials Youngs modulus, E_0, and some function, ϕ of material density, x_e, where $0 < x_e \leq 1$.

$$E_e = \phi(x_e)E_0 \tag{2.2}$$

If a density falls between 0 and 1 it is an intermediate density defined as neither solid or void. This is seen as grey elements in the final optimal design, and known as greyscale. To minimise or eliminate greyscale the function $\phi(x_e)$ is chosen such that during the optimization process each cell is forced either to solid or void phase by penalizing these intermediate densities. A number of penalization functions have been used throughout different literature, but

the most popular is that which was introduced by Bendsøe [29].

$$\phi(x_e) = {x_e}^p \tag{2.3}$$

$$E_e = {x_e}^p E_0 \tag{2.4}$$

where p is the penalization parameter. Bendsøe and Sigmund proved that this power law approach is valid when p is sufficiently large and should be selected at $p \geq 3$ [30].

There are a number of ways to model material distribution problems, the most common being SIMP and level-set methods. The level set method optimizes the the location of the material boundary where elements inside the boundary are given a material density of 1 and elements outside the boundary a material density of 0 [31]. This method requires the user to specify an initial boundary for the domain in order to control the length scale and level of detail found in the optimized domain. As a result this method is prone to converging to sub-optimal structures based on the initial guess [32]. This work uses the SIMP-based methods throughout as it is easier to avoid convergence at sub-optimal designs, but also because of the simplicity of implementing a SIMP-based method.

2.3 Numerical Instabilities

It has been noted that a number of numerical instabilities can arise when using a density-based topology optimization procedure [33, 34]. These instabilities stem from the numerical formulations used to solve the problem. Different instabilities can occur at different stages in the optimization problem. This section highlights potential instabilities and the steps taken to prevent them. To better understand these numerical instabilities we study the topology optimization of a simply supported beam subject to a unit load halfway across its span. The objective function is to minimize compliance subject to a volume constraint of 0.4. Unless otherwise stated the design domain is discretized into 120x20 elements. The design domain is shown in Figure 2.2.

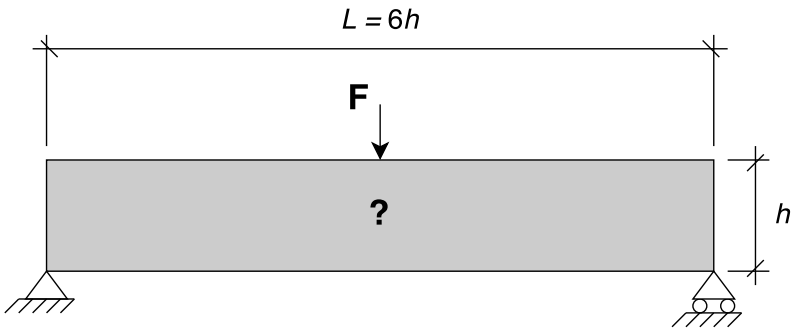

Figure 2.2: Design domain for the simply supported beam example problem.

2.3.1 Grayscale

Grayscale refers to converged designs where certain elements are not equal to either 0 or 1. These intermediate elements appear as gray in the final structure which gives rise to the name. This instability is mostly avoided due to the nature of the SIMP method as penalization encourages the optimizer to push material densities 0 or 1. The higher the penalization, the higher the bias towards 0-1 structure, and the less likely it is for grayscale to occur. However, choosing a higher penalization parameter can also encourage designs to converge to a local minimum (refer to Section 2.3.4). Figure 2.3 shows the solution to the simply supported beam problem without penalization.

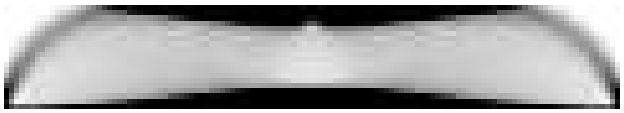

Figure 2.3: Simply supported beam solution without penalization.

2.3.2 Checkerboarding

Checkerboarding can occur when using 4-node quadrilateral elements. These elements allow load to be transferred from one element to another diagonally through a single common node which can cause the off-diagonal elements to become void. Hence, an infeasible geometry is created as there will be 0 thickness at the common node. If this occurs multiple times within the structure a solid-void checkered pattern is produced which gives rise to the name. Checkerboarding is depicted in the Figure 2.4. This solution implements a penalization parameter of 3 forcing it to converge to a 0-1 structure, unlike the solution in Figure 2.3.

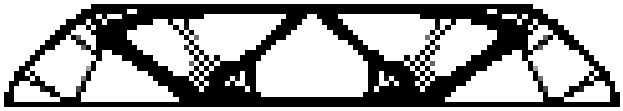

Figure 2.4: Simply supported beam solution containing checkerboarding.

There are number of techniques for eliminating checkerboarding in designs. As checkerboarding only occurs with 4-node quadrilateral elements one method is to use a higher-order order elements, such as 8-node quadrilaterals, however, this method greatly increases computational time. Another method is to define a mesh discretization such that single node connections can not occur. Menezes et al. implemented polygonal elements for topology optimization [35] and Zhou introduced a hybrid discretization to serve this purpose [36]. These methods increase the number of nodes or elements required, which in-turn also increases computational time. Another alternative approach is to implement patch [37] or restriction [38] methods, which produces groups of 4 or more elements into so called patches, and enforces constraints between patches.

Throughout this work we use a filtering method due to its simplicity and computational efficiency. This method is primarily implemented to handle the mesh dependency (refer to Section 2.3.3), however, it also solves the issue of checkerboarding. Filtering methods establish relationships between any one element and its surrounding elements. There are two basic types of filtering methods – density filtering [39, 40] and sensitivity filtering [1, 33]. Sensitivity filtering alters element sensitivities whereas density filtering alters element material densities. Density filtering is chosen for this work as it has the advantage of using the true sensitivities so we know the exact problem the optimization algorithm is solving. Refer to Section 3.2.2 for a detailed description on the filtering method. Figure 2.5 shows the solution to the simply supported beam problem with a density filter. By comparing this solution to Figure 2.4 we see that checkerboarding has been eliminated from the design.

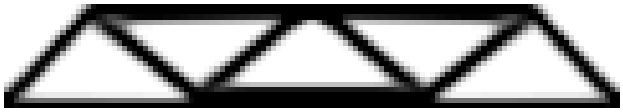

Figure 2.5: Simply supported beam solution with a density filter.

2.3.3 Mesh-Dependency

Mesh-dependence refers to the case where designs can change drastically with the coarseness of the finite element mesh. Very coarse meshes can produce inaccurate and unreliable finite element element results while a finer mesh can increase the complexity of topologies. Finer meshes can produce a large number of thin members which can increase the complexity, reduce the viability and reduce manufacturability of the design. Unless steps are taken to rectify this effect, drastically different designs will be achieved depending on the mesh used. Ultimately, this irregularity occurs because the physical description of the problem is ill-posed causing a nonexistence of solutions [33].

Parameter constraints can be used to control the sizing or number of structural members in optimal designs [33]. This in turn then addresses the issue of mesh-dependency. In this work however, we achieve mesh independence through density filtering (previous discussed in Section 2.3.2). For a more detailed description on density filtering refer to Section 3.2.2. Mesh-independence can be achieved with density filtering provided an appropriately sized filter radius is chosen. The filter radius should be determined based on the size of the domain and independent of the element size. It is also worth noting that density filters produce a gray fuzzy area around the material boundary. A comparison between mesh-dependent and mesh-independent designs is shown in Figure 2.6.

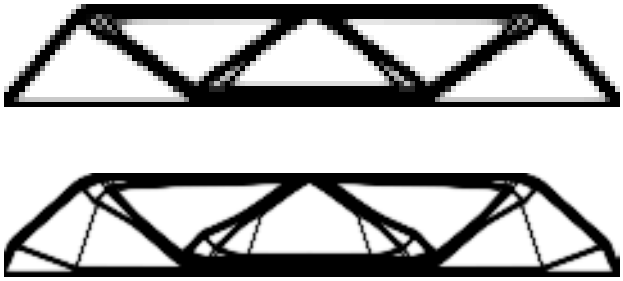

(a) Solutions with a small density filter spanning only adjacent elements. Coarse mesh (top) has 120x20 elements, fine mesh (bottom) has 240x40 elements

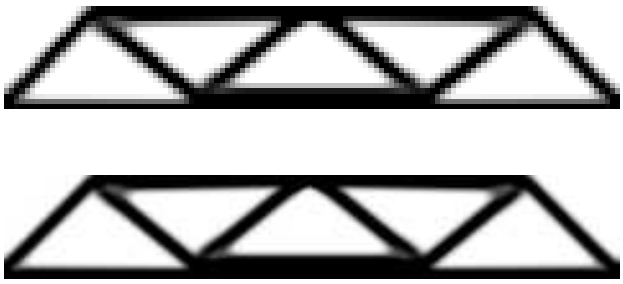

(b) Solutions with an appropriate density filter spanning equal distance regardless of element size. Coarse mesh (top) has 120x20 elements, fine mesh (bottom) has 240x40 elements

Figure 2.6: Comparison between (a) mesh-dependent designs with a small density filter and (b) mesh-independence designs with an appropriate density filter.

2.3.4 Local Minima

During the search for an optimal design the optimizer can on occasion converge to a design that is locally optimal but sub-optimal on the global scale. For non-convex design problems there may be a number of given designs within the design space that are minimal within some neighborhood surrounding those design points, but are not at a global minimum, i.e. there exists another point within the design space that will produce a better design. These points are called local minima and the minimum point in the entire design space is called the global minimum. This concept can easily be represented in three dimensional space with an optimization problem having an objective function, g, and two design variables, x_1 and x_2 (refer to Figure 2.7). Here the design space is represented by a surface that has two lower limit points. One of these points produces a lower value of g and hence is the optimal solution or global minimum. The other point is a local minimum and produces the best design within its local neighborhood but is sub-optimal throughout the entire design space.

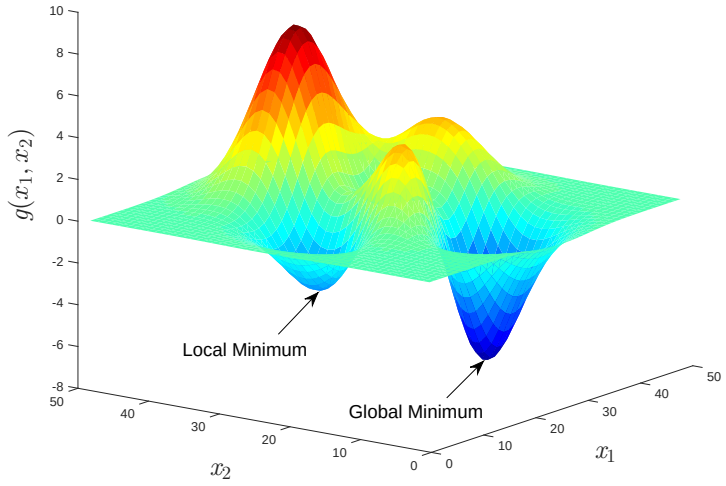

Figure 2.7: Design space for an objective function, $g(x_1, x_2)$, containing a local and global minimum.

In topology optimization the inclusion of the penalization parameter, p, makes the problem non-convex which can create local minima. In most non-convex optimization problems one can test whether their design is a local minimum by solving the optimization problem from different initial conditions. If the optimizer converges to multiple designs then it is known all but one of those designs is a local minimum (but does not guarantee the last design is a global minimum). In topology optimization there is a large number of design variables (at least one per element in the discretized mesh), meaning that to carry out such a procedure will require running a large number of simulations from different initial conditions, and so will not be suitable. However, when using a power law interpolation function (ϕ in Eqn. 2.2) we can ensure that optimal solutions can be produced if the initial conditions are neutral.

The penalization method creates a bias in the optimizer such that design variables are pushed to extreme values, i.e. $x \in \{0,1\}$. If a design variable, x, is equal to 0.2 the optimizer will be biased in moving the value of x towards 0. The same can said for $x = 0.8$, where the optimizer will be bias in pushing the value of x towards 1. This bias is created by the slope of the function, ϕ, and causes the optimizer to push design variables away from their ideal values for a globally optimal solution, and in turn converging to a sub-optimal design. To prevent these biases from impacting the solution it is important to select initial conditions that are as neutral as possible. Typically topology optimization problems are subject to a form of resource constraint (refer to Section 4.1.2). An appropriate neutral initial condition is to ensure this constraint is active and that all design variables are equal, i.e. for a resource constraint of 0.4, each design variable will have an initial conditions $x_{i=0} = 0.4$. Figure 2.8 shows two different initial conditions (top) and

their optimal solutions (bottom). Notice how a random material distribution for an initial condition converges to a sub-optimal solution (local minimum).

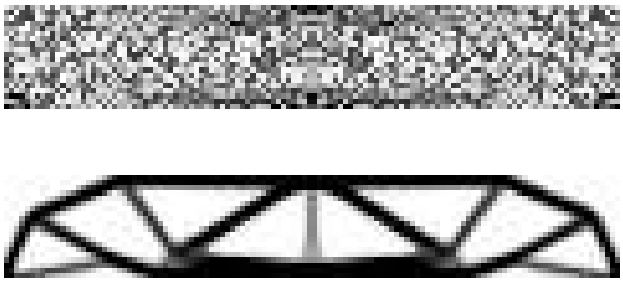

(a) Random initial material distribution (top) and corresponding converged solution (bottom).

(b) Neutral initial material distribution (top) and corresponding converged solution (bottom).

Figure 2.8: Comparison between converged solutions with (a) random initial material distribution and (b) neutral initial material distribution.

Another way to ensure convergence at a global minimum is through continuation methods [41, 42]. Continuation methods alter the optimization parameters incrementally over the course of solving the optimization problem. The most common continuation method is to alter the penalization parameter [10, 43, 44, 45]. Here an initial value of p is selected such to create little or no bias in the initial stages of optimization. As the problem develops the value of p is increased gradually to its target value. Implementing this method ensures the design variables are not prematurely pushed to the extreme values thus avoiding local minima. Another continuation method is adaptive filtering [1, 12] where the filter size is initially large and is slowly decreased to produce a 0-1 design. Alternatively a weighting function can be used to gradually increase cost of intermediate densities [46]

2.4 Manufacturing Considerations

Topology optimization methods were first developed over 40 years but only recently have started make an impact within industry [21, 22]. For example, Airbus have applied topology optimization to the design of leading edge ribs in the wings of their A380 airliner [47]. One reason why it has taken so long for these design methods to have an influence within industry comes with the developments in additive manufacturing. The flexibility of topology optimization as design method makes it perfect for additive manufacturing where complex geometry can easily be manufactured. However, manufacturing constraints should still be considered at the design stage.

Common manufacturing considerations include symmetric modeling, resource constraints, cyclic modeling, minimum member sizing constraints, minimum thickness constraints (to eliminate holes in 3D topology optimization) [48], and convolution filtering functions [49]. Minimum sizing constraints ensures that designs are created that can easily manufactured using traditional manufacturing methods [49, 50]. Cyclic modeling takes advantage of repetition in geometry of design problems such as the linear repetition of ribs in aircraft wings [47, 51] or circular repetition of spokes in a wheel [52, 53]. Symmetric modeling is similar to that of cyclic modeling where one takes advantage of the symmetry of design problem. These methods also vastly reduce computational time. Convolution filtering functions are used to produce clearer boundaries when using density based topology optimization. These filters implement a nonlinear relationship between weighting and distance from the filtered element, thus reducing the size of the gray smeared boundaries due to the filtering process. Resource constraints are cost constraints on the amount of material available for the design. This constraint keeps manufacturing costs low and in many cases (such as compliance minimization problems) prevents the optimization from becoming ill-posed. Refer to Section 4.1.2 for more on resource constraints. Symmetric modeling and resource constraints are the most common manufacturing considerations in topology optimization and will be implemented throughout this work.

Chapter 3

Mechanical Analysis

This chapter will detail the mechanical analysis used for both metallic and polymeric materials. Section 3.1 describes the process of conventional linear finite element analysis (FEA) and then expands this theory to nonlinear FEA. Section 3.2 describes discretization methods including introducing the formulation for modeling functionally graded materials and the filtering process. Stress-based design is summarized in Section 3.3.

3.1 Finite Element Analysis

Compliant mechanisms achieve movement through the deflection of structural members which can produce large strains during operation. With large strains it is important to ensure materials do not yield (or fail). Because of this polymeric materials are often suggested for compliant mechanism design as they can experience large strains without failing. These materials experience geometric nonlinearity which means the material response is non-linear due to large changes in geometry of the structure [54]. This also means that conventional linear FEA is no longer suitable for analysis of these materials. However, linear FEA is suitable for mechanical analysis of metallic materials as they experience a linear material response providing it does not yield. In this work, linear FEA is used in conjunction with stress constraints (to ensure the material does not yield) for the analysis of metallic mechanisms.

Polymeric hyperelastic materials experience a nonlinear load-displacement relationship within their elastic range. There are a number of examples in the literature nonlinear finite element analysis is used for topology optimization [39, 55, 56]. Sigmund et al. has demonstrated the importance of nonlinear analysis in compliant mechanism design through a comparison with linear designs [55]. This paper shows how drastically designs can change based on the finite element model, and even suggests a gain in performance up to a factor of 2.5 can be achieved with nonlinear vs. linear analysis. There are a number of hyperelastic models that can be used for this analysis as discussed in [57] [58], and some recent example where these are implemented for topology optimization include [45, 59, 60, 61].

3.1.1 Linear Finite Element Analysis

Linear finite element analysis is the standard for solving problems with metallic materials. These materials experience a linear elastic force-displacement relationship provided the material does not yield. This condition will be enforced with the use of a stress constraint. Stress-based design is discussed in more detail in Section 3.3. Given an external force distribution in the form a vector, **f**, a nodal displacement vector, **u**, can be determined via the following governing equation

$$\mathbf{R} = \mathbf{K}(\boldsymbol{x})\mathbf{u} - \mathbf{f} = 0 \tag{3.1}$$

where **K** is the stiffness matrix, which is a function of the design variables, $\boldsymbol{x}$, and is a global assembly of element stiffness matrices $\mathbf{k}_e$. Element stiffness matrices are calculated as follows

$$\mathbf{k}_e = \int_{\Omega_e} \bar{\mathbf{B}}^T \mathbf{D} \bar{\mathbf{B}} d\Omega_e \tag{3.2}$$

where $\bar{\mathbf{B}}$ is the strain-displacement matrix containing spatial derivatives of the shape functions, **N**, with respect to the coordinates, **x**. The constitutive matrix assumes plane stress and is represented by **D**. The term Ω_e represents that it is an integral over the element domain. Matrices $\bar{\mathbf{B}}$ and **D** are calculated using Eqn's 3.3 and 3.4 respectively.

$$\bar{\mathbf{B}} = \frac{\partial \mathbf{N}}{\partial \mathbf{x}} = \begin{bmatrix} \frac{\partial \mathrm{N}}{\partial \mathrm{x}}_{1,1} & 0 & \frac{\partial \mathrm{N}}{\partial \mathrm{x}}_{1,2} & 0 & \frac{\partial \mathrm{N}}{\partial \mathrm{x}}_{1,3} & 0 & \frac{\partial \mathrm{N}}{\partial \mathrm{x}}_{1,4} & 0 \\ 0 & \frac{\partial \mathrm{N}}{\partial \mathrm{x}}_{2,1} & 0 & \frac{\partial \mathrm{N}}{\partial \mathrm{x}}_{2,2} & 0 & \frac{\partial \mathrm{N}}{\partial \mathrm{x}}_{2,3} & 0 & \frac{\partial \mathrm{N}}{\partial \mathrm{x}}_{2,4} \\ \frac{\partial \mathrm{N}}{\partial \mathrm{x}}_{2,1} & \frac{\partial \mathrm{N}}{\partial \mathrm{x}}_{1,1} & \frac{\partial \mathrm{N}}{\partial \mathrm{x}}_{1,2} & \frac{\partial \mathrm{N}}{\partial \mathrm{x}}_{1,2} & \frac{\partial \mathrm{N}}{\partial \mathrm{x}}_{2,3} & \frac{\partial \mathrm{N}}{\partial \mathrm{x}}_{1,3} & \frac{\partial \mathrm{N}}{\partial \mathrm{x}}_{2,4} & \frac{\partial \mathrm{N}}{\partial \mathrm{x}}_{1,4} \end{bmatrix} \tag{3.3}$$

$$\mathbf{D} = \frac{E_e}{1-\nu^2} \begin{bmatrix} 1 & \nu & 0 \\ \nu & 1 & 0 \\ 0 & 0 & \frac{1}{2}(1-\nu) \end{bmatrix} \tag{3.4}$$

where E_e is the Young's modulus of the element and ν is the Poisson's ratio. Element stresses can then be determined using the strains, $\boldsymbol{\varepsilon}$.

$$\boldsymbol{\sigma} = \mathbf{D}\boldsymbol{\varepsilon} = \mathbf{D}\bar{\mathbf{B}}\mathbf{u}_e \tag{3.5}$$

3.1.2 Nonlinear Finite Element Analysis

Our analysis of polymeric materials is conducted using FEA for geometrically nonlinear hyperelastic materials. A hyperleastic material is one where the material status can completely be describable with a given total strain [57]. In

hyperelastic material models the potential energy function is represented as a function of deformation, and the stress can be obtained by differentiating the potential energy function with respect to deformation. Because of the elastic nature of these materials, the material model is independent of the deformation history, i.e. for the same final load the same deformation can be expected, and once the load is released the material will return to the unperturbed state. There are two types of models for hyperelastic materials – mechanistic models, which are based off the underlying structure of the material; and phenomenological models, which are based off empirical observations. Mechanistic models (e.g. Neo-Hookean, and Arruda-Boyce) require independent material properties, such as Young's modulus and Poisson's ratio. Phenomenological models (e.g. Ogden, Mooney-Rivlin, and Yeoh) require parameters for curve fitting the material response to the model [54, 62].

This section will detail the static response of hyperelastic materials based on the total Lagrangian formulation. For simplicity, we use the Neo-Hookean model as it requires only one material parameter [63], we then require less experimental testing to obtain the material properties (compared to other mechanistic models), and additional curve fitting parameters required for phenomenological models. 4-node isoparametric quadrilateral elements will be used throughout the analysis. The total Lagrangian method assumes a continuous mapping between coordinates in the undeformed state, $\mathbf{X}$, and the current (deformed) state, $\mathbf{x}$. The deformation gradient, $\mathbf{F}$, can then be defined as,

$$\mathbf{F} = \frac{\partial \mathbf{x}}{\partial \mathbf{X}} \tag{3.6}$$

From Eqn. 3.6 it then holds that $\mathbf{F}$ is equal to the inverse of the derivative of $\mathbf{X}$ with respect to $\mathbf{x}$. This derivative can be calculated using element nodal coordinates of the undeformed state, $\mathbf{X}$, and the derivative of the shape function, $\mathbf{N}$, with respect to the deformed geometry $\mathbf{x}$.

$$\mathbf{F} = \left(\frac{\partial \mathbf{X}}{\partial \mathbf{x}}\right)^{-1} = \left(\left[\frac{\partial \mathbf{N}}{\partial \mathbf{x}}\mathbf{X}\right]^{\mathrm{T}}\right)^{-1} = \left(\mathbf{X}^{\mathrm{T}}\frac{\partial \mathbf{N}}{\partial \mathbf{x}}^{\mathrm{T}}\right)^{-1} \tag{3.7}$$

The right and left Cauchy-Green deformation tensors ($\mathbf{C}$ and $\mathbf{B}$ respectfully) can then be defined in terms of the deformation gradient.

$$\mathbf{C} = \mathbf{F}^{\mathrm{T}}\mathbf{F} \tag{3.8}$$

$$\mathbf{B} = \mathbf{F}\mathbf{F}^{\mathrm{T}} \tag{3.9}$$

The compressible Neo-Hookean model is then used to solve the mechanics problem. As mentioned previously the potential energy function can be used to compute stresses within hyperelastic materials. For isotropic materials

the constitutive relation must be independent of the coordinate frame as the material properties are the same in all directions. This means that a strain component such as ε_{11} cannot be used for the constitutive relation since it is dependent on the coordinate system. Hence, the potential energy function is defined using Lamé constants and the right Cauchy-Green deformation tensor.

$$\Phi = \frac{1}{2}\lambda_0[\ln J]^2 - \mu_0 \ln J + \frac{1}{2}\mu_0[\mathrm{tr}(\mathbf{C}) - 3] \tag{3.10}$$

where J is computed as the determinant of $\mathbf{F}$. The term tr($\mathbf{C}$) denotes the trace of the right Cauchy-Green deformation tensor. Eqn. 3.10 utilizes the Lamé constants, μ_0 and λ_0, which can be represented in terms of the element's Young's modulus, E_e, and the Poisson's ratio, ν. For polymeric materials, tensile testing is conducted to obtain values for E and ν (refer to Appendix A).

$$\mu_0 = \frac{E_e}{2(1+\nu)} \tag{3.11}$$

$$\lambda_0 = \frac{\nu E_e}{(1+\nu)(1-2\nu)} \tag{3.12}$$

The Second Piola-Kirchoff stress, $\mathbf{S}$, can now be calculated as twice the derivative of the potential energy function with respect to the right Cauchy-Green deformation tensor.

$$\mathbf{S} = 2\frac{\partial \Phi}{\partial \mathbf{C}} = \lambda_0[\ln J]\mathbf{C}^{-1} + \mu_0(\mathbf{I} - \mathbf{C}^{-1}) \tag{3.13}$$

The Second Piola-Kirchoff stress relates forces in the reference configuration (undeformed state) with areas also measured in the reference configuration. From here we can now evaluate the Cauchy stress, $\boldsymbol{\sigma}$, which will relate forces in the current configuration (deformed state) with areas in the current configuration. The Cauchy stress is defined as

$$\boldsymbol{\sigma} = \frac{1}{J}\mathbf{F}\mathbf{S}\mathbf{F}^{\mathrm{T}} \tag{3.14}$$

and using Eqn. 3.13, can be calculated as

$$\begin{aligned} \boldsymbol{\sigma} &= \frac{1}{J}\left[\lambda_0[\ln J]\mathbf{I} + \mu_0(\mathbf{F}\mathbf{F}^{\mathrm{T}} - \mathbf{I})\right] \\ &= \frac{1}{J}\left[\lambda_0[\ln J]\mathbf{I} + \mu_0(\mathbf{B} - \mathbf{I})\right] \end{aligned} \tag{3.15}$$

By rearranging the Cauchy stress to Voigt notation, $\bar{\boldsymbol{\sigma}}$ (3×1 in two dimensions), the internal force of a given element can be calculated by

$$\mathbf{f}_{int,e} = \int_{\Omega_e} \bar{\mathbf{B}}^{\mathrm{T}} \bar{\boldsymbol{\sigma}} d\Omega_e \tag{3.16}$$

To keep structural equilibrium the internal and external forces must be balanced. This gives the global residual form as

$$\mathbf{R} = \mathbf{f}_{ext} - \mathbf{f}_{int} = \mathbf{0} \tag{3.17}$$

This residual equation gives rise to a nonlinear system of equations which are solved iteratively using a Newton-Raphson procedure to obtain the global vector of nodal displacements, $\mathbf{u}$ (refer to Section 3.1.3). During each iteration the nodal displacements are updated by $\Delta\mathbf{u}$ (until convergence of Eqn. 3.17) using the following linear system of equations

$$\mathbf{K}_{tan}\Delta\mathbf{u} = \mathbf{R} \tag{3.18}$$

The matrix $\mathbf{K}_{tan}$ is known as the tangent stiffness matrix and is formed by assembling element tangent stiffness matrices, $\mathbf{k}_{tan,e}$. The element tangent stiffness is calculated as a sum of a material and a geometric component as follows

$$\mathbf{k}_{tan,e} = \mathbf{k}_{tan,e}^{geo} + \mathbf{k}_{tan,e}^{mat} \tag{3.19}$$

$$\mathbf{k}_{tan,e} = \mathbf{I} \otimes \left(\int_{\Omega_e} \tilde{\mathbf{B}}^{\mathrm{T}} \boldsymbol{\sigma} \tilde{\mathbf{B}} d\Omega_e \right) + \int_{\Omega_e} \bar{\mathbf{B}}^{\mathrm{T}} \bar{\mathbf{D}} \bar{\mathbf{B}} d\Omega_e \tag{3.20}$$

where $\bar{\mathbf{D}}$ is the constitutive tensor which relating stress to strain (assuming plane strain) and is calculated via Eqn. 3.21, $\tilde{\mathbf{B}}$ is a special compact version of the strain displacement matrix, which retains only the nonzero entries from the original matrix, $\bar{\mathbf{B}}$. Note also that the operator $\otimes$, denotes the matrix outer product. These methods are further detailed in [57] and [58].

$$\bar{\mathbf{D}} = \begin{bmatrix} \lambda_0 + 2\mu_0 & \lambda_0 & 0 \\ \lambda_0 & \lambda_0 + 2\mu_0 & 0 \\ 0 & 0 & \mu_0 \end{bmatrix} \tag{3.21}$$

$$\tilde{\mathbf{B}} = \begin{bmatrix} \bar{\mathrm{B}}_{1,1} & \bar{\mathrm{B}}_{1,3} & \bar{\mathrm{B}}_{1,5} & \bar{\mathrm{B}}_{1,7} \\ \bar{\mathrm{B}}_{2,2} & \bar{\mathrm{B}}_{2,4} & \bar{\mathrm{B}}_{2,6} & \bar{\mathrm{B}}_{2,8} \end{bmatrix} \tag{3.22}$$

3.1.3 Displacement Control

Linear FEA only requires initial and final loading conditions to capture the material response. Geometric nonlinearity describes the case when there is a change in material behavior due to a change in geometry as the material is distorted. Thus the material behavior changes with displacement and iterative procedures are required to fully capture the material response. Either a prescribed force or displacement is increased iteratively to the final desired load/displacement, where a system of linear equations is solved (Eqn. 3.18) on each iteration to capture discrete points of the material response. When modeling a nonlinear material response it is often necessary to implement displacement control. If the material response curve (i.e. force-displacement curve) contains limit points then the response cannot be fully defined using force control as a single force may correspond to multiple different displacement values. This will give multiple solutions to Eqn. 3.18 at that specific degree of freedom (DOF). This causes numerical issues when inverting the Jacobian matrix due to the appearance of severe mesh distortion which leads the FEA to diverge. Figure 3.1 shows (a) a linear material response and (b) a nonlinear material response, both of which can be fully defined by any given force value. The third figure, (c), depicts a nonlinear material response that cannot be fully defined by any given force as f_2 corresponds to two different displacements values. However, in (c) the displacement can be used to fully define the material response as each displacement corresponds to only one force value.

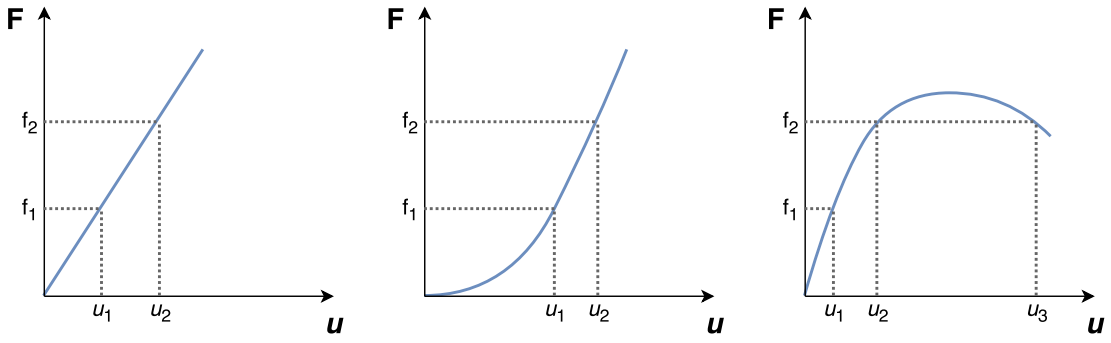

Figure 3.1: Comparison between (a) linear material response, (b) nonlinear material response, (c) nonlinear material response with limit point.

As the topology of the structure changes on each iteration of the optimizer, the material response can vary dramatically over the course of the optimization. To ensure stability in the mechanical analysis we adopt a displacement control method. This Newton-Raphson based method was first introduced by Batoz and Dhatt in [64]. We prescribe one non-zero displacement and the aim is to solve for all unknowns in the problem, namely all unspecified displacements, and the magnitude of the external force, θ, required to create the specified non-zero displacement. The external

force used in Eqn. 3.17 is defined as

$$\mathbf{f}_{ext} = \theta \mathbf{f}_0 \tag{3.23}$$

where $\mathbf{f}_0$ is a sparse reference vector of size equal to the number of DOF and a unit value at the DOF corresponding to the applied force. This method uses a decomposed tangent stiffness matrix introduced in Eqn. 3.18. Eqn. 3.18 can be expressed as

$$\mathbf{K}_{tan}[\Delta\mathbf{u}^a \mid \Delta\mathbf{u}^b] = [\mathbf{R} \mid \mathbf{f}_0] \tag{3.24}$$

where $\mathbf{u}_a$ and $\mathbf{u}_b$ are defined as

$$\mathbf{u} = \mathbf{u}^a + \theta \mathbf{u}^b \tag{3.25}$$

and so

$$\Delta\mathbf{u} = \Delta\mathbf{u}^a + \Delta\theta\Delta\mathbf{u}^b \tag{3.26}$$

The above system of equations is solved on each iteration until convergence of the residual equation (Eqn. 3.17). The displacement at the prescribed input degree of freedom, p, is incremented by $\Delta \mathrm{u}_p$ at the start of each iteration. Using nested iterative procedure we seek a self-correcting $\Delta\mathbf{u}$ such that Eqn. 3.17 is satisfied. As the displacement at p is specified at the start of each outer iteration, we want no change in displacement at p for inner loop iteration, i. From Eqn. 3.26 we get

$$[\Delta \mathrm{u}_p]^i = [\Delta \mathrm{u}_p^a]^i + \Delta\theta^i [\Delta \mathrm{u}_p^b]^i = 0 \tag{3.27}$$

$$\Delta\theta^i = -\frac{[\Delta \mathrm{u}_p^a]^i}{[\Delta \mathrm{u}_p^b]^i} \tag{3.28}$$

These values are the self-correcting increments for the displacement field and input force, i.e.

$$[\mathbf{u}]^{i+1} = [\mathbf{u}]^i + [\Delta\mathbf{u}]^{i+1} \tag{3.29}$$

$$\theta^{i+1} = \theta^i + \Delta\theta^i \tag{3.30}$$

This process is repeated for the desired number of outer iterations until convergence of Eqn. 3.17 when u_p is equal to the desired input displacement. This method is useful for topology optimization due to the subsequent use of the decompose tangent stiffness matrix in sensitivity analysis (Section 4.2) and its quadratic convergence.

3.2 Discretization

The entire design domain is discretized into finite elements, where each element has a material density, $\boldsymbol{x}$. The material density is used as a parameter to determine which elements should be included in the design, and which should be excluded. The goal is to achieve a clear 0-1 structure at convergence where the element, e, belongs to the structure if its material density, x_e, is equal to 1 and void for x_e equal to 0. To produce a clear converged solution the material density for the elements must be forced to either 0 or 1. This is achieved using the SIMP (solid isotropic material with penalization) method [29, 65]. This is a gradient based approach that penalizes material properties that relate to the Young's modulus.

$$E_e = x_e^p E_0 \implies \lambda_e = x_e^p \lambda_0 \quad ; \quad \mu_e = x_e^p \mu_0 \tag{3.31}$$

In the above, the subscript e indicates that the property is specific to an element. The element density raised to the power of p, multiplied by the material property for a solid material gives the effective material property for the penalized material. The penalization parameter, p, is chosen to be 3 throughout this work. By penalizing intermediate material densities (raised to the power of p) a solid-void design is promoted during optimization.

Traditionally in topology optimization we require the material densities to range between zero and one. However, by specifying a minimum material density of zero the FEA can diverge when inverting the Jacobian matrix (a procedure common to both linear and nonlinear FEA analysis). If elements are at or close to zero stiffness it can cause excessive mesh distortion and irregular or overlapping of elements. This in-turn creates numerical issues as the Jacobian matrix becomes singular and the FEA problem unsolvable. To cope with this a minimum material density value, $\boldsymbol{x}_{min}$, is selected to be close enough to zero so that void regions have minimal impact in FEA results, but not too small that the solution procedure diverges. Note that this method is not used in the functionally graded case as the SIMP method is defined differently to cope with this problem.

3.2.1 FGM Formulation

We implement an original SIMP-type formulation for representing the local element material properties in the FGM problem. This method is similar to those adopted in [12] and [13] where each element is assigned two design variables. The effective Young's modulus is evaluated as follows

$$E_e = E_{min} + x_{0,e}^{p}\left(E_l + x_{1,e}(E_u - E_l)\right) \tag{3.32}$$

where the subscript *min* denotes the minimum allowable modulus value, l and u denote the lower and upper modulus limits, $x_{0,e}$ is the material density of the element e and is penalized such that $x_{0,e} \in \{0,1\}$ for all e at a converged result. The second design variable, $x_{1,e}$, is the mixing ratio between upper and lower bounds of the Young's modulus, which is not penalized such that $0 \leq x_{1,e} \leq 1$, thus promoting an unbiased material distribution. The addition of the term E_{min} ensures that there is some stiffness in the void regions, therefore $x_{0,min} = 0$ for the functionally graded case. Note that the mixing ratios, $\boldsymbol{x_1}$, are computational design variables and do not represent the physical mixing ratio between materials. The physical mixing ratio (for manufacture) will be determined based on the local Young's modulus in converged designs. Also note that in order to compare homogeneous and FGM mechanisms, the minimum modulus must be equal for the two cases i.e. $E_{min} = {x_{min}}^{p} E_0$.

3.2.2 Filtering

Density filters alter the density of each element by producing a relationship between an element's material density and the material density of its surrounding elements. A density filter matrix, $\boldsymbol{W}$ is defined such that

$$\tilde{\boldsymbol{x}} = \boldsymbol{W}\boldsymbol{x} \tag{3.33}$$

where $\tilde{\boldsymbol{x}}$ is a vector of filtered or physical variables and $\boldsymbol{x}$ contains the independent variables. For the homogeneous case, the independent variables are the material densities, whereas in the FGM case, the independent variables include both material densities and mixing ratios. In the FGM case, Young's modulus, E, is also filtered to ensure smooth gradations throughout the structure. Physical variables produce the final structure and are used in FEA, whereas the sensitivities are calculated with respect to the independent variables. A filter radius, r, is used to determine how many of the surrounding elements will contribute to the density filter. For any element, e, a circle of radius r is traced with its center at e's centroid. All other elements whose centroid lie within this radius contribute to the material density of e. Element contributions are weighted such that the closer the neighboring element the higher the weighting will be. For this work we use a linear relationship between the weighting and the distance between element centroids. All elements outside the filter radius carry no weight. This relationship can be represented as a cone with its center coincident to the centroid of e and the weighting of other elements is defined by the height of the cone above their respective centroid, see Figure 3.2. The entries in $\boldsymbol{W}$, w_{ij}, are calculated as

$$\bar{w_{ij}} = \max[0, r - d_{ij}] \tag{3.34}$$

$$w_{ij} = \frac{1}{\sum_{k=1}^{N_r} w_{\bar{ij},k}} \bar{w_{ij}} \tag{3.35}$$

where the subscript ij denotes the i^{th} row and j^{th} column, r is the filter radius and d_{ij} is the distance between the two element centroids, N_r is the number of elements whose centroids lie within the filter radius. Eqn. 3.35 normalizes the entries of $\boldsymbol{W}$ calculated in Eqn. 3.34 such that the rows of $\boldsymbol{W}$ sum to 1.

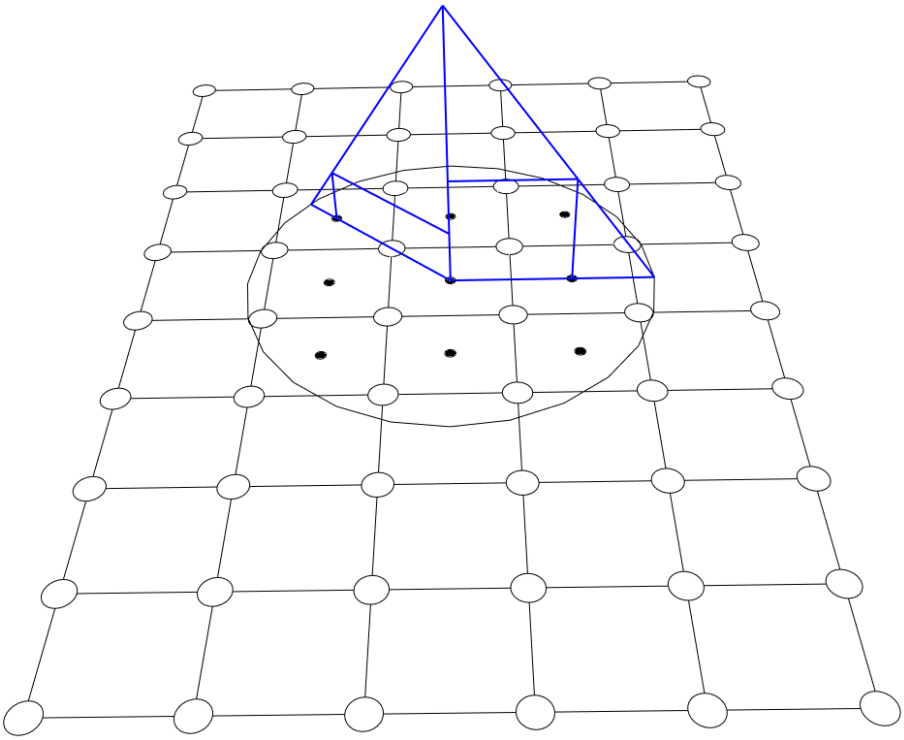

Figure 3.2: Cone representation of the filtering process.

3.3 Stress Based Design

In the past, stress constraints have been introduced into topology optimization design to produce designs that are not vulnerable to failure [66, 67, 68, 69]. Compliant mechanisms incorporate thin compliant joints to achieve movement, however, these thin members also create stress concentrations in the design. Stress concentrations are areas of increased stress caused by irregular geometry such as thin members, curves or sharp corners. For this work we will implement stress constraints based on the von Mises yield criterion.

The von Mises yield criterion is an empirical method of determining whether a material will yield when subjected to complex loading. Von Mises proposed the method in 1913 [70] and in 1931 Taylor and Quinney [71] found that the method is a more accurate predictor for yielding in metals than any previous suggested methods, such as Tresca's maximum yield stress criterion [72]. The von Mises stress crterion states that a material will fail if the von Mises stress exceeds the material's yield stress. The von Mises stress is defined in terms of plane stress in Eqn. 3.36.

$$\sigma_{VM} = \sqrt{{\sigma_{xx}}^2 - \sigma_{xx}\sigma_{yy} + {\sigma_{yy}}^2 + 3{\sigma_{xy}}^2} \tag{3.36}$$

where σ_{xx}, σ_{yy}, σ_{xy} are calculated as the entries in Eqn. 3.5 (linear FEA) or 3.15 (nonlinear FEA). The von Mises stress is calculated at the 4 Gauss points of an element and averaged to obtain the von Mises stress within the element.

The von Mises stress yield criterion is still the most commonly adopted method for failure prediction used today, although it is not without some shortcomings. As an empirical formulation there is no strict relation between when the von Mises criterion predicts yielding, and when yielding actually occurs, however it has been proven to work successfully as a predictor. Another major drawback is that the von Mises stress is always positive and therefore it does not hold any information about whether the material is compression, tension or pure shear. Yield stress is commonly determined from tensile testing as it is the easiest method. However, in real-world applications, materials generally experience a difference between yield in tension and compression [73]. This is called the strength-differential (SD) effect and has been shown experimentally in the past [74, 75, 76]. For the majority of materials the compressive yield stress is higher than their tensile yield stress. This means that the von Mises stress criterion can indicate a material in compression has yielded prematurely. This causes issues in enforcing stress constraints for certain designs. As yield strength is most commonly found through tensile testing there is limited availability of compressive yield strength over the broad range of materials necessary for our FGM formulation. Instead, we handle the issue caused by the SD effect by making regions we know to experience high stress due to compression exempt from the constraint. Refer to Section 5.2 for a more detailed description of this design procedure.

Chapter 4

Optimization Approach

4.1 Design Problem Definitions

This section details the objective functions and constraints used in the optimization process. Throughout this work two different objective functions have been used and are subject to up to three different constraints – a resource constraint, a compliance constraint, and a stress constraint.

4.1.1 Objective Functions

In Eqn. 2.1 we show how to define an optimization problem. When designing compliant mechanisms the objective function is generally defined in one of two ways – to maximize mechanical advantage, or to maximize geometric advantage. Mechanical advantage is the ratio of the output force to in input force, whereas geometric advantage is the ratio of output displacement to input displacement. Our objective function is defined as follows

$$\begin{aligned} g(\mathbf{u}(\boldsymbol{x}),\mathbf{f}(\boldsymbol{x}),\boldsymbol{x}) &= \frac{F_{out}}{F_{in}} \quad \text{for Mechanical Adv.} \\ &= \frac{u_{out}}{u_{in}} \quad \text{for Geometric Adv.} \end{aligned} \tag{4.1}$$

4.1.2 Resource Constraint

The resource constraint is defined in Eqn. 4.2, where $M(\boldsymbol{x})$ can be either the local volume or Young's modulus, which are both a function of the independent variables, i.e. a volume or modulus constraint is used – these constraints will be described in more detail further on. The maximum value of M that is physically possible for the entire design domain, Ω, is denoted as M_0. The ratio of $M(\boldsymbol{x})$ to M_0 is summed over Ω to give the resource fraction (volume or modulus fraction, refer to Eqn's 4.4 and 4.5). This ratio must be less than or equal to some user prescribed allowance, $\bar{M}$. Note also that the volume and modulus fractions are equal for the homogeneous case as the Young's modulus is constant for each element.

$$\int_{\Omega} \frac{M(\boldsymbol{x})}{M_0} d\Omega - \bar{M} \leq 0 \tag{4.2}$$

For the homogeneous case the resource fraction can be calculated in Eqn. 4.3. The domain is assumed to have a uniform thickness, t, and an area, A_{Ω}, consisting of N_e elements of area A_e. As all elements are of equal size, Eqn. 4.3 reduces to the sum of material densities divided by the number of elements, N_e.

$$\int_{\Omega} \frac{M(\boldsymbol{x})}{M_0} d\Omega = \frac{1}{A_{\Omega} t x_{max}} \sum_{e=1}^{N_e} A_e t x_e = \frac{1}{N_e} \sum_{e=1}^{N_e} x_e \tag{4.3}$$

For functionally graded meterials when a volume constraint is used the resource fraction is expressed as a volume fraction similar to that of the homgoeneous case, and following the same theory the resource fraction is calculated as follows.

$$\int_{\Omega} \frac{M(\boldsymbol{x})}{M_0} d\Omega = \frac{1}{N_e} \sum_{e=1}^{N_e} x_{0,e} \tag{4.4}$$

Note that this constraint is evaluated purely based on $x_{0,e}$ and so elements with a higher Young's modulus have the same cost as those with a lower Young's modulus. However, when a modulus constraint is used, elements of a higher Young's modulus come at a greater cost than those of a lower Young's modulus. This encourages designs with a wider spectrum of Young's modulus values. The resource fraction is calculated by Eqn. 4.5 when a modulus constraint is used.

$$\int_{\Omega} \frac{M(\boldsymbol{x})}{M_0} d\Omega = \frac{1}{N_e E_u} \sum_{e=1}^{N_e} E_e \tag{4.5}$$

4.1.3 Compliance Constraint

The second constraint is a compliance constraint, which is imposed at the input for the mechanical advantage problem and the output for the geometric advantage problem. This constraint ensures that there is a continuous chain of material between the point of application and the boundary conditions. Because the objective function is a ratio, it can continuously be minimized by lowering the output (for positive g) or input (for negative g), which in-turn prompts

optimizer to solve this irregularity by reducing element densities at input/output locations. By ensuring some level of stiffness at the input/output locations (i.e. not void), the force must be large enough to overcome the resistance produced. Alternatively a minimum value constraint can be imposed on the input force for the gripper or output displacement for the inverter, but this will not necessarily guarantee the continuous chain of material as elements can still be pushed to void. The compliance constraint is defined in Eqn. 4.6a when using force control, and in Eqn. 4.6b when using displacement control

$$C - C_{max} \leq 0 \tag{4.6a}$$

$$C_{min} - C \leq 0 \tag{4.6b}$$

where C is the compliance of the mechanism, C_{max} and C_{min} are the maximum and minimum allowable values for compliance for the mechanism, i.e. an upper bound is used for force control and a lower bound for displacement control.

4.1.4 Stress Constraint

The mechanical analysis of metals can be solved accurately using linear finite element analysis provided that the material does not yield. To ensure materials do not yield enforce a stress constraint on the mechanism such that the von Mises stress is less than yield stress for each element in the design domain.

$$\sigma_{VM} \leq \sigma_y \tag{4.7a}$$

$$\sigma_{VM} \leq \sigma_y(E_e) \tag{4.7b}$$

where Eqn. 4.7a represents the homogeneous case as yield stress, σ_y is constant, where as 4.7b represents the FGM case where σ_y is a function of the local Young's modulus, E_e, as it is a local material property. We normalize the Young's modulus to provide a better representation for comparison between different FGM yield strength relationships (refer to Section 5.2 for more details).

Von Mises stress is calculated using strain, and so areas in the mesh with high strain will experience high stresses. The highest strains may occur in void regions and so it is possible for the highest stresses to also occur in void regions. To prevent this, we employ stress relaxation such that the constraint becomes

$$x^{\eta}\left(\frac{\sigma_{VM}}{\sigma_y}-1\right)-\varepsilon\leq 0 \tag{4.8a}$$

$$x_0{}^{\eta}\left(\frac{\sigma_{VM}}{\sigma_{y,E_e}}-1\right)\leq 0 \tag{4.8b}$$

where σ_{y,E_e} is the value of σ_y evaluated with the element's value of E_e. In using this formulation, stresses are relaxed in the element by multiplying by the material density raised to the exponential η, which is chosen to be 0.5. By relaxing the stresses in this manner, higher stresses can occur in void regions without violating the stress constraint, such that only the solid regions must satisfy $\sigma_{VM}\leq\sigma_y$. The constraint function also incorporates the term, ε, which is a constant subtracted from the relaxed homogeneous stress function. This term is included in the homogeneous case because the minumum value of x is not equal to zero meaning the function is conservative. This is not an issue for the FGM formulation because the minimum value of x_0 is 0, and so ε is not included. The value of ε is chosen to be$\sqrt{x_{min}}$.

The constraint function in Eqn. 4.8 must be satisfied for each element in the design mesh. This presents us with a very large number of design constraints which will be computationally expensive. Instead we choose to focus on the element where the stress is highest. To find the element with maximum stress we use the p-norm function which gives the final constraint functions for homogeneous and FGM designs as

$$\left[\sum_{e=1}^{N_e}\left(x_e{}^{\eta}\frac{\sigma_{VM}}{\sigma_y}\right)^{\zeta}\right]^{\frac{1}{\zeta}}-(1+\varepsilon)\leq 0 \tag{4.9a}$$

$$\left[\sum_{e=1}^{N_e}\left(x_{0,e}{}^{\eta}\frac{\sigma_{VM}}{\sigma_{y,E_e}}\right)^{\zeta}\right]^{\frac{1}{\zeta}}-1\leq 0 \tag{4.9b}$$

where ζ is a constant used to evaluate the p-norm and is chosen to be 10.

4.2 Sensitivity Analysis

Sensitivity analysis is conducted to determine how each design variable should vary between iterations in order to move towards an optimal design. Sensitivities are required for the objective function and all the constraints used in the design. The majority of these functions hold both explicit and implicit dependence on $\boldsymbol{x}$. In these design problems there is a large ratio of design variables to constraint functions. This makes the adjoint method ideal for calculating the sensitivities. We can express any function, F, in augmented Lagrangian form as follows

$$\Pi_F = F + \boldsymbol{\lambda}^{\mathrm{T}}\mathbf{R} = F + \begin{bmatrix} \boldsymbol{\lambda}_f{}^{\mathrm{T}} & \boldsymbol{\lambda}_p{}^{\mathrm{T}} \end{bmatrix} \begin{bmatrix} \mathbf{R}_f \\ \mathbf{R}_p \end{bmatrix} \tag{4.10}$$

where F can represent any objective or constraint function, $\boldsymbol{\lambda}$ is the Lagrangian multiplier, whose values must be determined. However, note that for any $\boldsymbol{\lambda}$, $\Pi_F = F$ as we know the residual, $\mathbf{R}$, is equal to 0 (refer to Eqn's 3.1 and 3.17). This equation can also be represented in terms of free and prescribed degrees of freedom (DOF) denoted by the subscripts f and p respectively. We require the sensitivities of the function with respect to each design variable, which is represented in vector form as the derivative of Π with respect to x. Using the chain rule we obtain the expression

$$\begin{aligned} \frac{d\Pi_F}{d\boldsymbol{x}} = \frac{\partial F}{\partial \boldsymbol{x}} + \frac{\partial F}{\partial \mathbf{u}_f}\frac{d\mathbf{u}_f}{d\boldsymbol{x}} + \frac{\partial F}{\partial \mathbf{f}_p}\frac{d\mathbf{f}_p}{d\boldsymbol{x}} + \boldsymbol{\lambda}_f{}^{\mathrm{T}}\left[\frac{\partial \mathbf{R}_f}{\partial \boldsymbol{x}} + \frac{\partial \mathbf{R}_f}{\partial \mathbf{u}_f}\frac{d\mathbf{u}_f}{d\boldsymbol{x}} + \frac{\partial \mathbf{R}_f}{\partial \mathbf{f}_p}\frac{d\mathbf{f}_p}{d\boldsymbol{x}}\right] \\ + \boldsymbol{\lambda}_p{}^{\mathrm{T}}\left[\frac{\partial \mathbf{R}_p}{\partial \boldsymbol{x}} + \frac{\partial \mathbf{R}_p}{\partial \mathbf{u}_f}\frac{d\mathbf{u}_f}{d\boldsymbol{x}} + \frac{\partial \mathbf{R}_p}{\partial \mathbf{f}_p}\frac{d\mathbf{f}_p}{d\boldsymbol{x}}\right] \end{aligned} \tag{4.11}$$

Together, $\mathbf{u}_f$ and $\mathbf{f}_p$ are the solutions to the finite element analysis. Note that the sixth term on the right hand side (RHS) of Eqn. 4.11 is always equal to zero as the residual at the free DOF have no dependence on the force at the prescribed DOF, and similarly the ninth term is always $\mathbf{1}$ (vector of ones). Note also the difference between $\frac{\partial}{\partial \boldsymbol{x}}$ and $\frac{d}{d\boldsymbol{x}}$ operators, which represent explicit and implicit derivatives respectively. Explicit derivatives capture only direct dependence of the function, whereas the implicit derivatives also capture indirect dependence due to the solution of the equilibrium equation (Eqn's 3.1 and 3.17 for linear and nonlinear analysis respectfully). We seek a $\boldsymbol{\lambda}$ that causes all implicit terms to vanish. The following subsections will detail derivations of the sensitivities for objective functions and each constraint function.

4.2.1 Objective Functions

Neither of the advantage functions has a direct dependence on the design variables and so the first term on the RHS of Eqn. 4.11 is equal to zero. Likewise, the second and third terms on the RHS are equal to zero for the mechanical

and geometric advantage problems respectively. This yields the following

$$\frac{d\Pi_g}{d\boldsymbol{x}} = \frac{\partial g}{\partial \mathbf{f}_p}\frac{d\mathbf{f}_p}{d\boldsymbol{x}} + \boldsymbol{\lambda}_f{}^{\mathrm{T}}\left[\frac{\partial \mathbf{R}_f}{\partial \boldsymbol{x}} + \frac{\partial \mathbf{R}_f}{\partial \mathbf{u}_f}\frac{d\mathbf{u}_f}{d\boldsymbol{x}}\right] + \boldsymbol{\lambda}_p{}^{\mathrm{T}}\left[\frac{\partial \mathbf{R}_p}{\partial \boldsymbol{x}} + \frac{\partial \mathbf{R}_p}{\partial \mathbf{u}_f}\frac{d\mathbf{u}_f}{d\boldsymbol{x}} + \frac{d\mathbf{f}_p}{d\boldsymbol{x}}\right] \tag{4.12a}$$

$$\frac{d\Pi_g}{d\boldsymbol{x}} = \frac{\partial g}{\partial \mathbf{u}_f}\frac{d\mathbf{u}_f}{d\boldsymbol{x}} + \boldsymbol{\lambda}_f{}^{\mathrm{T}}\left[\frac{\partial \mathbf{R}_f}{\partial \boldsymbol{x}} + \frac{\partial \mathbf{R}_f}{\partial \mathbf{u}_f}\frac{d\mathbf{u}_f}{d\boldsymbol{x}}\right] + \boldsymbol{\lambda}_p{}^{\mathrm{T}}\left[\frac{\partial \mathbf{R}_p}{\partial \boldsymbol{x}} + \frac{\partial \mathbf{R}_p}{\partial \mathbf{u}_f}\frac{d\mathbf{u}_f}{d\boldsymbol{x}} + \frac{d\mathbf{f}_p}{d\boldsymbol{x}}\right] \tag{4.12b}$$

where Eqn's 4.12a and 4.12b are for mechanical and geometric advantages respectively. To make all implicit derivative vanish we choose $\boldsymbol{\lambda}$ as follows

$$\begin{aligned} \boldsymbol{\lambda}_p{}^{\mathrm{T}} &= -\frac{\partial g}{\partial \mathbf{f}_p} \\ \boldsymbol{\lambda}_f{}^{\mathrm{T}} &= -\boldsymbol{\lambda}_p{}^{\mathrm{T}}\frac{\partial \mathbf{R}_p}{\partial \mathbf{u}_f}\left[\frac{\partial \mathbf{R}_f}{\partial \mathbf{u}_f}\right]^{-1} = -\boldsymbol{\lambda}_p{}^{\mathrm{T}}\mathbf{K}_{pf}\mathbf{K}_{ff}^{-1} \end{aligned} \tag{4.13a}$$

$$\begin{aligned} \boldsymbol{\lambda}_p{}^{\mathrm{T}} &= \mathbf{0} \\ \boldsymbol{\lambda}_f{}^{\mathrm{T}} &= -\frac{\partial g}{\partial \mathbf{u}_f}\left[\frac{\partial \mathbf{R}_f}{\partial \mathbf{u}_f}\right]^{-1} = -\frac{\partial g}{\partial \mathbf{u}_f}\mathbf{K}_{ff}^{-1} \end{aligned} \tag{4.13b}$$

where Eqn. 4.13*a* and 4.13*b* are for objective functions of mechanical and geometric advantage respectively. The stiffness matrix, or tangent stiffness matrix (linear vs. nonlinear), $\mathbf{K}/\mathbf{K}_{tan}$, is also partitioned where $\mathbf{K}_{pf}$ is the matrix whose rows and columns are equal to the prescribed and free DOF of $\mathbf{K}/\mathbf{K}_{tan}$. Likewise $\mathbf{K}_{ff}$ is the matrix whose rows and columns are equal free-free DOF of $\mathbf{K}/\mathbf{K}_{tan}$. The final adjoint sensitivity then becomes

$$\begin{aligned} \frac{d\Pi_g}{d\boldsymbol{x}} &= \boldsymbol{\lambda}_p{}^{\mathrm{T}}\frac{\partial \mathbf{R}_p}{\partial \boldsymbol{x}} + \boldsymbol{\lambda}_f{}^{\mathrm{T}}\frac{\partial \mathbf{R}_f}{\partial \boldsymbol{x}} = \boldsymbol{\lambda}^{\mathrm{T}}\frac{\partial \mathbf{R}}{\partial \boldsymbol{x}} \\ \implies \frac{d\Pi_g}{dx} &= \boldsymbol{\lambda}_e{}^{\mathrm{T}}\frac{\partial \mathbf{R}}{\partial x} \end{aligned} \tag{4.14}$$

where $\boldsymbol{\lambda}$ and $\boldsymbol{\lambda}_e$ can contain entries from both fixed and prescribed DOF. The derivative of the residual is calculated as the derivative of Eqn. 3.1 for linear analysis and Eqn. 3.17 for nonlinear analysis. In Eqn. 3.17 the external force has no direct dependence on $\boldsymbol{x}$, therefore the derivative of the residual with respect to $\boldsymbol{x}$ is equal to the negative of the internal force differentiated with respect to $\boldsymbol{x}$.

$$\frac{\partial \mathbf{R}}{\partial x} = \frac{\partial \mathbf{k}_e}{\partial x}\mathbf{u}_e = px^{p-1}\mathbf{k}_0\mathbf{u}_e \tag{4.15a}$$

$$\begin{aligned} \frac{\partial \mathbf{R}}{\partial x} &= -\frac{\partial}{\partial x}\left(\int_{\Omega_e} \bar{\mathbf{B}}^{\mathrm{T}}\bar{\boldsymbol{\sigma}}\, d\Omega_e\right) \\ \frac{\partial \mathbf{R}}{\partial x} &= \int_{\Omega_e} \bar{\mathbf{B}}^{\mathrm{T}}\left(\frac{1}{J}\left[\frac{\partial \lambda_e}{\partial x}[\ln J]\mathbf{I} + \frac{\partial \mu_e}{\partial x}(\mathbf{B}-\mathbf{I})\right]\right) \end{aligned} \tag{4.15b}$$

where Eqn's 4.15a and 4.15b are for linear and nonlinear analysis respectively. The term $\mathbf{k}_0$ is calculated via Eqn 3.2 without penalizing E_e in Eqn. 3.4. Derivatives in Eqn. 4.15b can be calculated for homogeneous and FGM cases ad follows

$$\begin{aligned} \frac{\partial \mu_e}{\partial x} &= px^{p-1}\frac{E_0}{2(1+\nu)} \\ \frac{\partial \lambda_e}{\partial x} &= px^{p-1}\frac{\nu E_0}{(1+\nu)(1-2\nu)} \end{aligned} \tag{4.16a}$$

$$\begin{aligned} \frac{\partial \mu_e}{\partial x} &= px_0{}^{p-1}\frac{E_l + x_1(E_u - E_l)}{2(1+\nu)} && \text{for } x \in \boldsymbol{x}_0 \\ &= x_0{}^{p}\frac{E_u - E_l}{2(1+\nu)} && \text{for } x \in \boldsymbol{x}_1 \\ \frac{\partial \lambda_e}{\partial x} &= px_0{}^{p-1}\frac{\nu(E_l + x_1(E_u - E_l))}{(1+\nu)(1-2\nu)} && \text{for } x \in \boldsymbol{x}_0 \\ &= x_0{}^{p}\frac{\nu(E_u - E_l)}{(1+\nu)(1-2\nu)} && \text{for } x \in \boldsymbol{x}_1 \end{aligned} \tag{4.16b}$$

4.2.2 Resource Constraints

The sensitivity of the resource constraints can be calculated by directly differentiating Eqn's 4.3, 4.4 and 4.5.

$$\frac{d}{dx}\left(\int_{\Omega}\frac{M(\boldsymbol{x})}{M_0}d\Omega\right) = \frac{1}{N_e} \tag{4.17a}$$

$$\frac{d}{dx}\left(\int_\Omega \frac{M(\boldsymbol{x})}{M_0}d\Omega\right) = \frac{1}{N_e} \quad \text{for } x \in \boldsymbol{x}_0$$
$$= 0 \quad \text{for } x \in \boldsymbol{x}_1 \tag{4.17b}$$

$$\frac{d}{dx}\left(\int_\Omega \frac{M(\boldsymbol{x})}{M_0}d\Omega\right) = \frac{p{x_0}^{p-1}(E_l + x_1(E_u - E_l))}{N_e(E_u + E_{min})} \quad \text{for } x \in \boldsymbol{x}_0$$
$$= \frac{{x_0}^p(E_u - E_l)}{N_e(E_u + E_{min})} \quad \text{for } x \in \boldsymbol{x}_1 \tag{4.17c}$$

where Eqn. 4.17a, 4.17b and 4.17c are for homogeneous, volume and Young's modulus constraints respectively.

4.2.3 Compliance Constraint

Sensitivity of the compliance constraint is calculated using the adjoint method. The theory remains the same as that adopted for the objective functions, where Eqn. 4.11 is simplified to Eqn. 4.18 and $\boldsymbol{\lambda}$ is defined in Eqn. 4.19.

$$\frac{d\Pi_C}{d\boldsymbol{x}} = \frac{\partial C}{\partial \mathbf{u}_f}\frac{d\mathbf{u}_f}{d\boldsymbol{x}} + \frac{\partial C}{\partial \mathbf{f}_p}\frac{d\mathbf{f}_p}{d\boldsymbol{x}} + {\boldsymbol{\lambda}_f}^{\mathrm{T}}\left[\frac{\partial \mathbf{R}_f}{\partial \boldsymbol{x}} + \frac{\partial \mathbf{R}_f}{\partial \mathbf{u}_f}\frac{d\mathbf{u}_f}{d\boldsymbol{x}}\right] + {\boldsymbol{\lambda}_p}^{\mathrm{T}}\left[\frac{\partial \mathbf{R}_p}{\partial \boldsymbol{x}} + \frac{\partial \mathbf{R}_p}{\partial \mathbf{u}_f}\frac{d\mathbf{u}_f}{d\boldsymbol{x}} + \frac{d\mathbf{f}_p}{d\boldsymbol{x}}\right] \tag{4.18}$$

$$\begin{aligned} {\boldsymbol{\lambda}_p}^{\mathrm{T}} &= \mathbf{u}_p \\ {\boldsymbol{\lambda}_f}^{\mathrm{T}} &= -\lambda_p \frac{\partial C}{\partial \mathbf{u}_f}\left[\frac{\partial \mathbf{R}_f}{\partial \mathbf{u}_f}\right]^{-1} = -\mathbf{u}_p \mathbf{K}_{pf}\mathbf{K}_{ff}^{-1} \end{aligned} \tag{4.19}$$

where $\mathbf{u}_p$ contains the prescribed input displacements. Similarly to Eqn. 4.14 we calculate the total sensitivity by assembling local element sensitivities via Eqn. 4.20, where $\frac{\partial \mathbf{R}}{\partial x}$ is calculated using Eqn. 4.15.

$$\begin{aligned} \frac{d\Pi_C}{d\boldsymbol{x}} &= {\boldsymbol{\lambda}_p}^{\mathrm{T}}\frac{\partial \mathbf{R}_p}{\partial \boldsymbol{x}} + {\boldsymbol{\lambda}_f}^{\mathrm{T}}\frac{\partial \mathbf{R}_f}{\partial \boldsymbol{x}} = \boldsymbol{\lambda}^{\mathrm{T}}\frac{\partial \mathbf{R}}{\partial \boldsymbol{x}} \\ \implies \frac{d\Pi_C}{dx} &= {\boldsymbol{\lambda}_e}^{\mathrm{T}}\frac{\partial \mathbf{R}}{\partial x} \end{aligned} \tag{4.20}$$

4.2.4 Stress Constraint

The adjoint method is also used to solve for the sensitivities of the stress constraint. For this constraint there is a direct dependence on the design variables so the first term on the RHS of Eqn 4.11 is not equal to zero, and so becomes

$$\frac{d\Pi_S}{d\boldsymbol{x}} = \frac{\partial S}{\partial \boldsymbol{x}} + \frac{\partial S}{\partial \mathbf{u}_f}\frac{d\mathbf{u}_f}{d\boldsymbol{x}} + \boldsymbol{\lambda}_f{}^{\mathrm{T}}\left[\frac{\partial \mathbf{R}_f}{\partial \boldsymbol{x}} + \frac{\partial \mathbf{R}_f}{\partial \mathbf{u}_f}\frac{d\mathbf{u}_f}{d\boldsymbol{x}}\right] + \boldsymbol{\lambda}_p{}^{\mathrm{T}}\left[\frac{\partial \mathbf{R}_p}{\partial \boldsymbol{x}} + \frac{\partial \mathbf{R}_p}{\partial \mathbf{u}_f}\frac{d\mathbf{u}_f}{d\boldsymbol{x}} + \frac{d\mathbf{f}_p}{d\boldsymbol{x}}\right] \tag{4.21}$$

where S represents the stress constraint function defined in Eqn. 4.9. The explicit derivative of S is calculated in Eqn. 4.22 while the Lagrangian multipliers are calculated via in Eqn. 4.23, utilizing the derivative of the stress constraint with respect to the displacement of free DOF expressed in Eqn. 4.24. Note that in Eqn's 4.22 and 4.24 the suffixes a and b represent homogeneous and FGM cases respectively, and σ_{y,E_e} is the yield stress for an element evaluated using its Young's modulus, E_e.

$$\frac{\partial S}{\partial x} = \left(x^{\eta}\frac{\sigma_{VM}}{\sigma_y}\right)^{\zeta}\left(\sum_{e=1}^{N_e}\left(x_e{}^{\eta}\frac{\sigma_{VM}}{\sigma_y}\right)^{\zeta}\right)^{\frac{1}{\zeta}-1}\left(\frac{\eta}{x} + \frac{1}{\sigma_{VM}}\frac{\partial \sigma_{VM}}{\partial x}\right) \tag{4.22a}$$

$$\begin{aligned}\frac{\partial S}{\partial x} &= \left(x_0{}^{\eta}\frac{\sigma_{VM}}{\sigma_{y,E_e}}\right)^{\zeta}\left(\sum_{e=1}^{N_e}\left(x_{0,e}{}^{\eta}\frac{\sigma_{VM}}{\sigma_{y,E_e}}\right)^{\zeta}\right)^{\frac{1}{\zeta}-1}\left(\frac{\eta}{x_0} + \frac{1}{\sigma_{VM}}\frac{\partial \sigma_{VM}}{\partial E_e}\frac{\partial E_e}{\partial x_0} - \frac{1}{\sigma_{y,E_e}}\frac{\partial \sigma_{y,E_e}}{\partial E_e}\frac{\partial E_e}{\partial x_0}\right) \quad \text{for } x \in \boldsymbol{x}_0 \\ &= \left(x_0{}^{\eta}\frac{\sigma_{VM}}{\sigma_{y,E_e}}\right)^{\zeta}\left(\sum_{e=1}^{N_e}\left(x_{0,e}{}^{\eta}\frac{\sigma_{VM}}{\sigma_{y,E_e}}\right)^{\zeta}\right)^{\frac{1}{\zeta}-1}\left(\frac{1}{\sigma_{VM}}\frac{\partial \sigma_{VM}}{\partial E_e}\frac{\partial E_e}{\partial x_1} - \frac{1}{\sigma_{y,E_e}}\frac{\partial \sigma_{y,E_e}}{\partial E_e}\frac{\partial E_e}{\partial x_1}\right) \quad \text{for } x \in \boldsymbol{x}_1\end{aligned} \tag{4.22b}$$

$$\begin{aligned}\boldsymbol{\lambda}_p{}^{\mathrm{T}} &= 0 \\ \boldsymbol{\lambda}_f{}^{\mathrm{T}} &= -\frac{\partial S}{\partial \mathbf{u}_f}\left[\frac{\partial \mathbf{R}_f}{\partial \mathbf{u}_f}\right]^{-1} = -\frac{\partial S}{\partial \mathbf{u}_f}\mathbf{K}_{ff}^{-1}\end{aligned} \tag{4.23}$$

$$\frac{\partial S}{\partial \mathbf{u}_f} = \frac{1}{\sigma_y{}^{\zeta}}\left(\sum_{e=1}^{N_e}\left(x_e{}^{\eta}\frac{\sigma_{VM}}{\sigma_y}\right)^{\zeta}\right)^{\frac{1}{\zeta}-1}\left(\sum_{e=1}^{N_e} x_e{}^{\zeta\eta}\sigma_{VM}{}^{\zeta-1}\frac{\partial \sigma_{VM}}{\partial \mathbf{u}_f}\right) \tag{4.24a}$$

$$\frac{\partial S}{\partial \mathbf{u}_f} = \frac{1}{\sigma_{y,E_e}{}^{\zeta}}\left(\sum_{e=1}^{N_e}\left(x_{0,e}{}^{\eta}\frac{\sigma_{VM}}{\sigma_{y,E_e}}\right)^{\zeta}\right)^{\frac{1}{\zeta}-1}\left(\sum_{e=1}^{N_e} x_{0,e}{}^{\zeta\eta}\sigma_{VM}{}^{\zeta-1}\frac{\partial \sigma_{VM}}{\partial \mathbf{u}_f}\right) \tag{4.24b}$$

We can now represent Eqn. 4.21 as follows, where $\frac{\partial \mathbf{R}}{\partial x}$ is calculated using Eqn. 4.15

$$\frac{d\Pi_S}{d\boldsymbol{x}} = \frac{\partial S}{\partial \boldsymbol{x}} + \boldsymbol{\lambda}_p{}^{\mathrm{T}} \frac{\partial \mathbf{R}_p}{\partial \boldsymbol{x}} + \boldsymbol{\lambda}_f{}^{\mathrm{T}} \frac{\partial \mathbf{R}_f}{\partial \boldsymbol{x}}$$
$$\implies \frac{d\Pi_S}{dx} = \frac{\partial S}{\partial x} + \boldsymbol{\lambda}_e{}^{\mathrm{T}} \frac{\partial \mathbf{R}}{\partial \boldsymbol{x}} \tag{4.25}$$

4.3 Optimization Algorithm

The optimization problem is solved using a gradient-based algorithm, namely the Method of Moving Asymptotes (MMA), outlined in [77]. During each optimization iteration the algorithm constructs and solves a convex approximation of the problem based on the current value and gradients of the Lagrangian. The solution of the convex sub-problem then becomes the updated design point in the optimization search. The design problem is said to have reached an optimal solution once the Karush-Kuhn-Tucker (KKT) conditions are satisfied [78, 79].

The complete algorithm combines methods discussed in Chapters 3 and 4. This algorithm is represented by the flowchart in Figure 4.1.

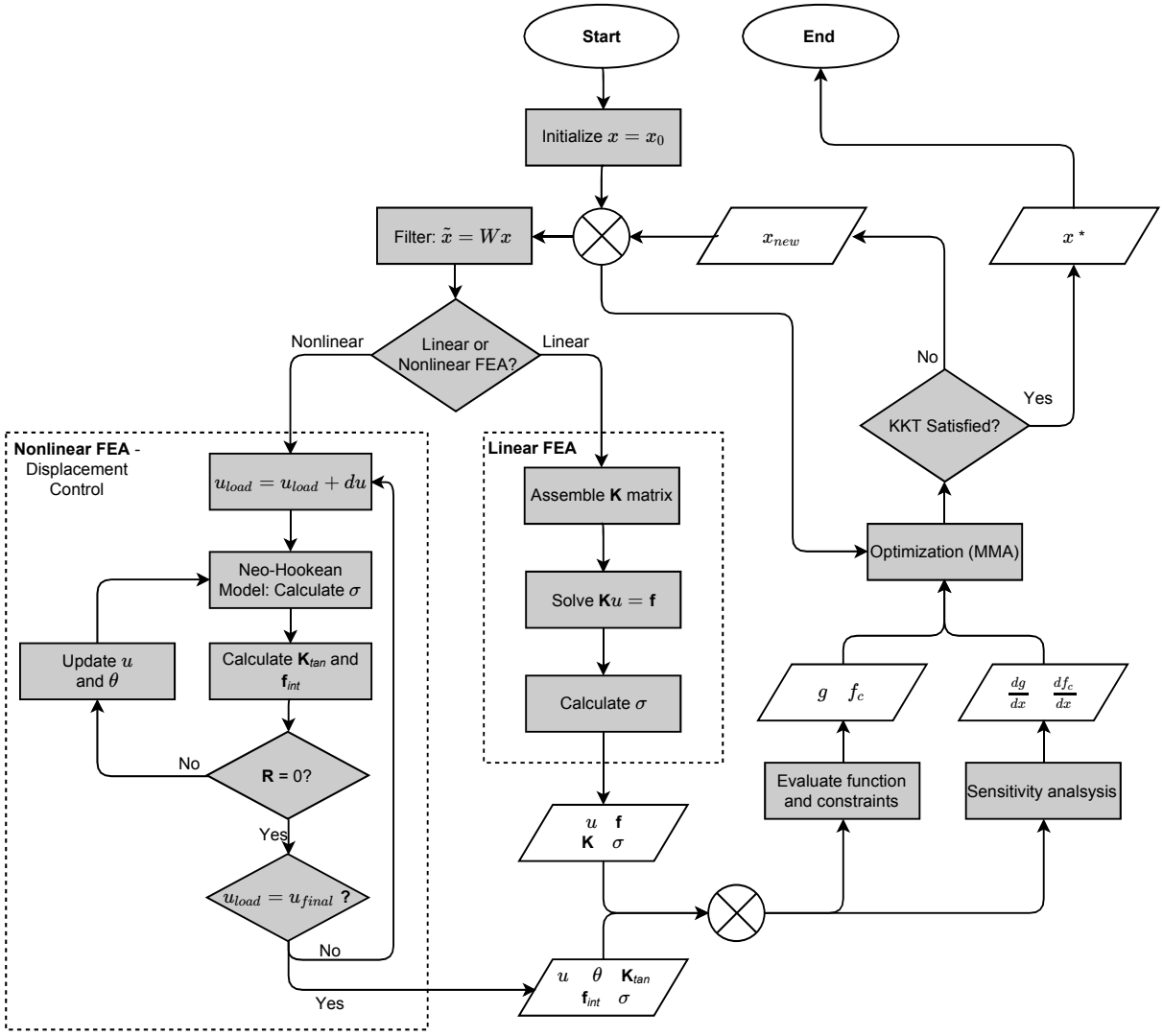

Figure 4.1: Flowchart of the complete algorithm use in this analysis.

4.4 Post-Optimization Analysis

Once designs have converged to an optimal structure we seek to produce more reliable results. As mentioned previously, void elements must have some stiffness during the optimization process to prevent the finite element analysis from diverging due to excessive mesh distortion (refer to Section 3.2). Even though void regions are modeled as a very compliant material, the presence of this extra stiffness in the mechanism alters the final result. Because of this, void elements in the optimized structure are removed from the finite element mesh and analysis is conducted on the new mesh to obtain new results. It is expected that these results are closer to the physical mechanical/geometric advantages that can be achieved after manufacturing. Where possible we also aim to verify the results through experimentally

testing the prototypes.

To define a boundary between void and solid regions we select a tolerance value, x_{tol}, such that elements are void if $x<x_{tol}$ for homogeneous designs, where $x_{tol} = 0.3$. For FGM designs, the structure is defined using Young's modulus, E, and so the boundary is defined based on a Young's modulus tolerance, E_{tol}, of 0.14 where elements are void if $E<E_{tol}$. Refer to Zegard and Paulino [49] for methods on creating clear material-void boundaries in density-based topology optimized designs with density filtering.

Chapter 5

Results

5.1 Design of Polymeric Compliant Mechanisms

This section details the design of two different types of polymeric compliant mechanism – a gripper, and a geometric inverter. The function of a gripper is to produce a mechanical advantage when gripping a workpiece, whereas an inverter aims to produce a displacement (or force) in the opposite direction to the input while producing some geometric (or mechanical) advantage. For the purpose of this analysis the gripper will produce a mechanical advantage while inverter produces a geometric advantage. The design domains of both problems are outlined in Figure 5.1. Due to the symmetry of the problem only half the domain is modeled. An input displacement, u_{in}, is prescribed at the left center of the design domains. At this input the nonlinear FEA code solves the resulting force to create this displacement. The output is specified at the right of the design domains and the structures are to be fixed at the top and bottom left corners of the domain. It is assumed that the gripper will act on a rigid workpiece and hence there will be no displacement at the output. Therefore, the output force will be equal to the negative of the reaction force at the output.

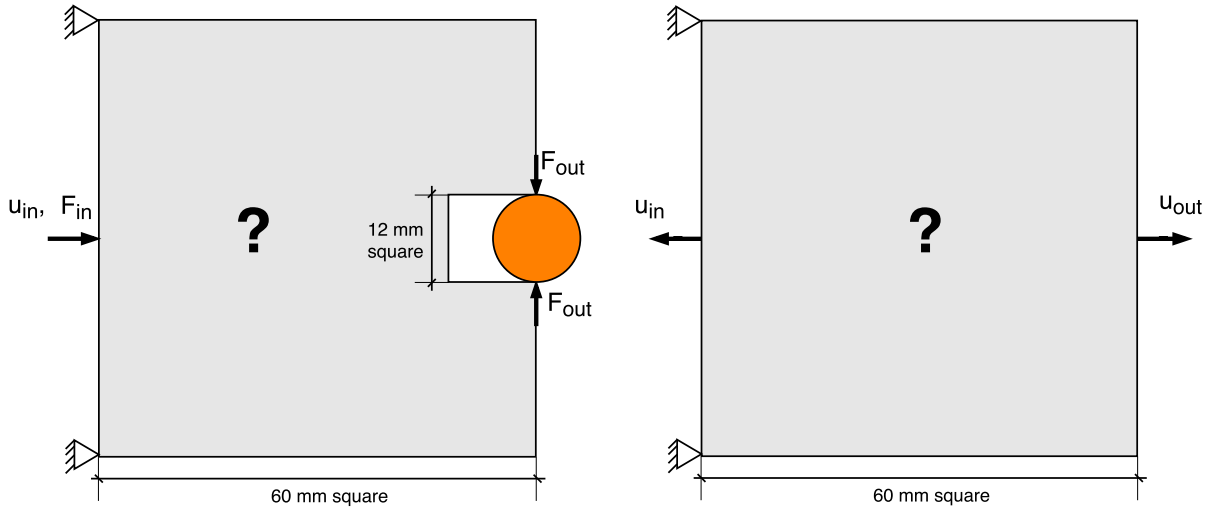

(a) Gripper design domain

(b) Inverter design domain

Figure 5.1: The two polymeric design problems illustrating boundary conditions, inputs, outputs and dimensions.

The purpose of these designs is to maximize the mechanical (case a) or geometric (case b) advantage. The design problem is defined below where the objective function, g, is subject to a resource and compliance constraint (refer to Section 4.1).

$$\begin{aligned}
\min_{x} \quad & : \quad g(\mathbf{u}(\boldsymbol{x}),\mathbf{f}(\boldsymbol{x}),\boldsymbol{x}) \quad = \frac{F_{out}}{F_{in}} \quad \text{(case a)} \\
& \qquad\qquad\qquad\qquad\quad = \frac{u_{out}}{u_{in}} \quad \text{(case b)} \\
\text{subject to} \quad & : \quad \int_{\Omega} \frac{M(\boldsymbol{x})}{M_0} d\Omega - \bar{M} \leq 0 \\
& : \quad C_{min} - C \leq 0 \\
& : \quad \mathbf{0} < \boldsymbol{x}_{min} \leq \boldsymbol{x} \leq \mathbf{1}
\end{aligned} \tag{5.1}$$

5.1.1 Case a: Gripper problem

Each gripper problem is solved for a unit input displacement (1 mm) and a larger displacement equal to 8% the design domain length (5 mm). Firstly the mechanical analysis problem is solved for the homogeneous case (whether the problem itself is homogeneous or functionally graded) with all element densities equal and a resource fraction of $\bar{M}$. Under this scenario the compliance of the structure is calculated and taken to be the minimum possible value of compliance, C_{min} (refer to Eqn. 5.1). All gripper results are presented with a resource constraint, $\bar{M}$, of 0.4. The design problem is detailed in Figure 5.1a and has an objective function to maximize mechanical advantage. Functionally

graded mechanisms were modeled in two different ways – firstly a volume constraint is used which only accounts for $\boldsymbol{x}_0$, and secondly we implemented a modulus constraint which accounts for values of both $\boldsymbol{x}_0$ and $\boldsymbol{x}_1$ (refer to Eqn. 3.32). Material properties used in the analysis were found experimentally (refer to Appendix A). All mechanisms have a Poisson's ratio of 0.4 with a Young's modulus of 11 MPa for homogeneous designs, while the local Young's modulus is optimally varied between 0.14 MPa and 11 MPa for FGM designs. Figures 5.2 and 5.3 show results for gripper designs with 1 mm and 5 mm input displacements respectively. Table 5.1 compares the mechanical advantage and maximum von Mises stress for all 6 gripper designs.

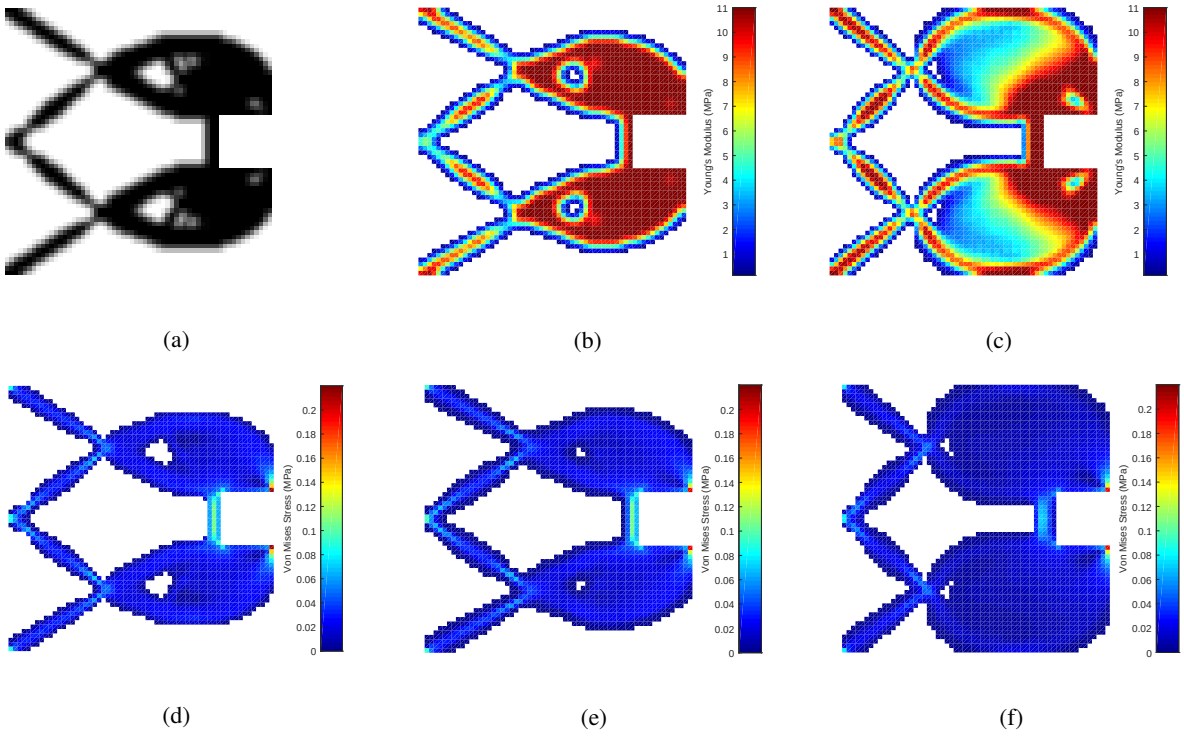

Figure 5.2: Gripper results for 1 mm input displacement. Converged topologies are shown on top – (a) homogeneous design, (b) FGM design with a volume constraint, (c) FGM design with a Young's modulus constraint. Von Mises stress distributions are shown on bottom – (d) homogeneous design, (e) FGM design with a volume constraint, (f) FGM design with a Young's modulus constraint.

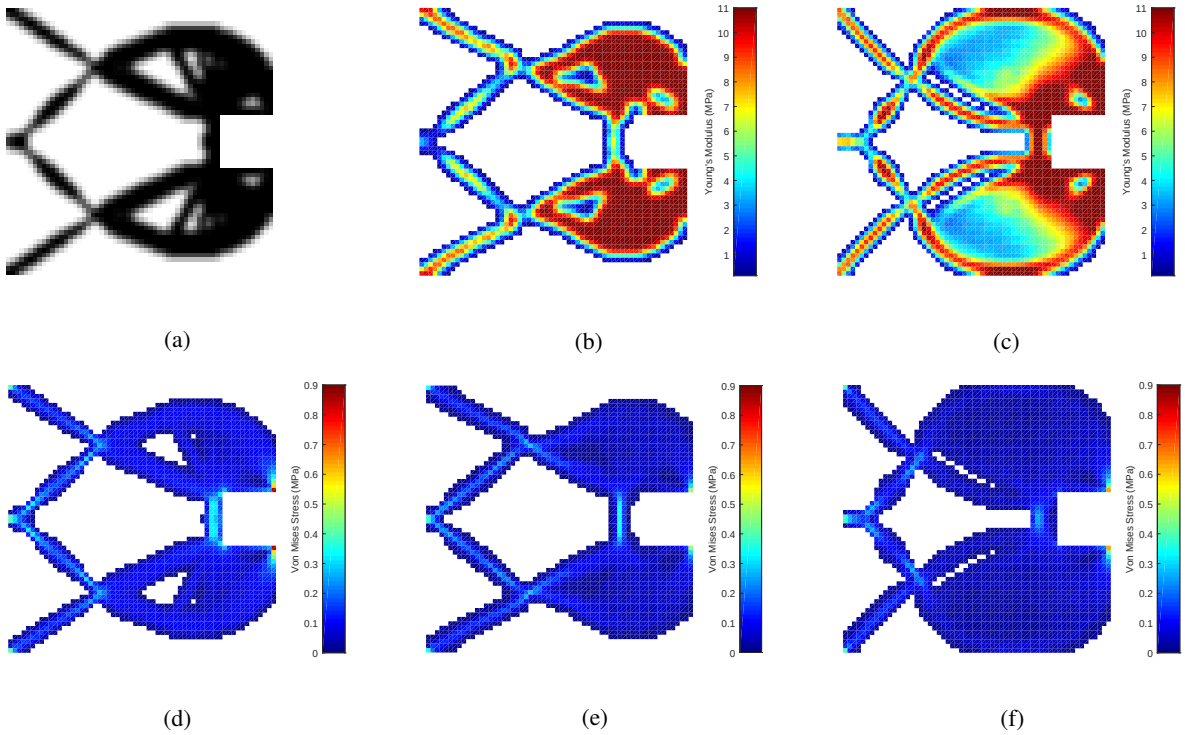

Figure 5.3: Gripper results for 5 mm input displacement. Converged topologies are shown on top – (a) homogeneous design, (b) FGM design with a volume constraint, (c) FGM design with a Young's modulus constraint. Von Mises stress distributions are shown on bottom – (d) homogeneous design, (e) FGM design with a volume constraint, (f) FGM design with a Young's modulus constraint.

			Void elements included		Void elements removed	
Material	***u_{in} (mm)***	***Constraint***	***Mech. Adv.***	***Max VM (MPa)***	***Mech. Adv.***	***Max VM (MPa)***
Homogeneous	1	-	2.22	0.211	2.39	0.206
FGM	1	Volume	2.04	0.193	1.63	0.186
FGM	1	Modulus	2.37	0.194	2.39	0.194
Homogeneous	5	-	1.88	0.858	3.55	0.833
FGM	5	Volume	1.11	0.452	1.63	0.535
FGM	5	Modulus	1.55	0.638	2.86	0.708

Table 5.1: Comparison between gripper results with the optimized mesh. This mesh models void regions with a very low stiffness.

In each gripper problem the maximum von Mises stress was reduced when FGMs were used, which suggests that FGM designs experience lower stresses than homogeneous designs. However, in some examples the mechanical advantage of the mechanism is also reduced with FGM designs. The largest loss in mechanical advantage is experienced when a volume constraint is used, but this design also produces the largest reduction in von Mises stresses. The modulus-constrained gripper produced a higher mechanical advantage than the homogeneous gripper for low displacement designs, but a lower mechanical advantage when optimized for higher outputs.

From the stress distributions we see that for all gripper designs the highest von Mises stress occurs at the output and the second highest at the input and boundary conditions. These stress concentrations are prominent in all designs and are an unavoidable for the mechanical advantage problem. The next largest stress concentration is at the back of the gripper's jaws, as seen in all examples. By comparing stress distributions for each design problem we see that FGM mechanisms have reduced the size and magnitude of these stress concentrations, particularly in the modulus-constrained designs. Stress concentrations also occur at the mechanism's compliant joints. When using a volume constraint, the FGM mechanism experiences stress magnitudes at the joints similar to that of the homogeneous mechanism, however, when using a modulus constraint these stresses are reduced.

Based on these results it can be said that by varying the material properties across the gripper mechanism, the von Mises stresses can be reduced as more compliant materials are optimally positioned throughout the structure. However, the algorithm is optimizing to maximize the mechanical advantage for which the inclusion of more compliant materials can also produce negative effects. These compliant elements will deform easier than stiffer elements which can lower reaction forces.

New meshes were then created with all void elements removed from the mesh (refer to Section 4.4). Mechanical analysis was conducted once more on the new meshes and the results are shown in Table 5.1. It is important to notice that results can change drastically when void elements are removed. We remove elements because it is expected that these results will be closer to physical values after manufacturing. Values of $x_{tol} = 0.3$ and $E_{tol} = 0.14$ were used to define the boundary of the material domain for homogeneous and FGM designs respectively. The same basic observations previously stated can also be drawn from these results, however removing void elements had different effect on different designs. The most significant changes appear in problems with larger deflections, which is expected as higher deflections will push further into void regions. Concentrating on the larger deflection mechanisms, we see that the mechanical advantage increases drastically for homogeneous (89% increase) and modulus-constrained (85% increase) mechanisms, but has less of an impact on the volume-constrained mechanism (47% increase). There was a small decrease in maximum von Mises stress in these mechanisms also.

The large displacement mechanisms that have been prototyped are shown in undeformed and deformed configurations in Figure 5.4. Unfortunately we do not have the capabilities to efficiently test the mechanical advantage of these mechanisms as this would require highly sensitive load cells on input and output ports. These devices will also have to be physically small in size in order to fit between the jaws of the gripper.

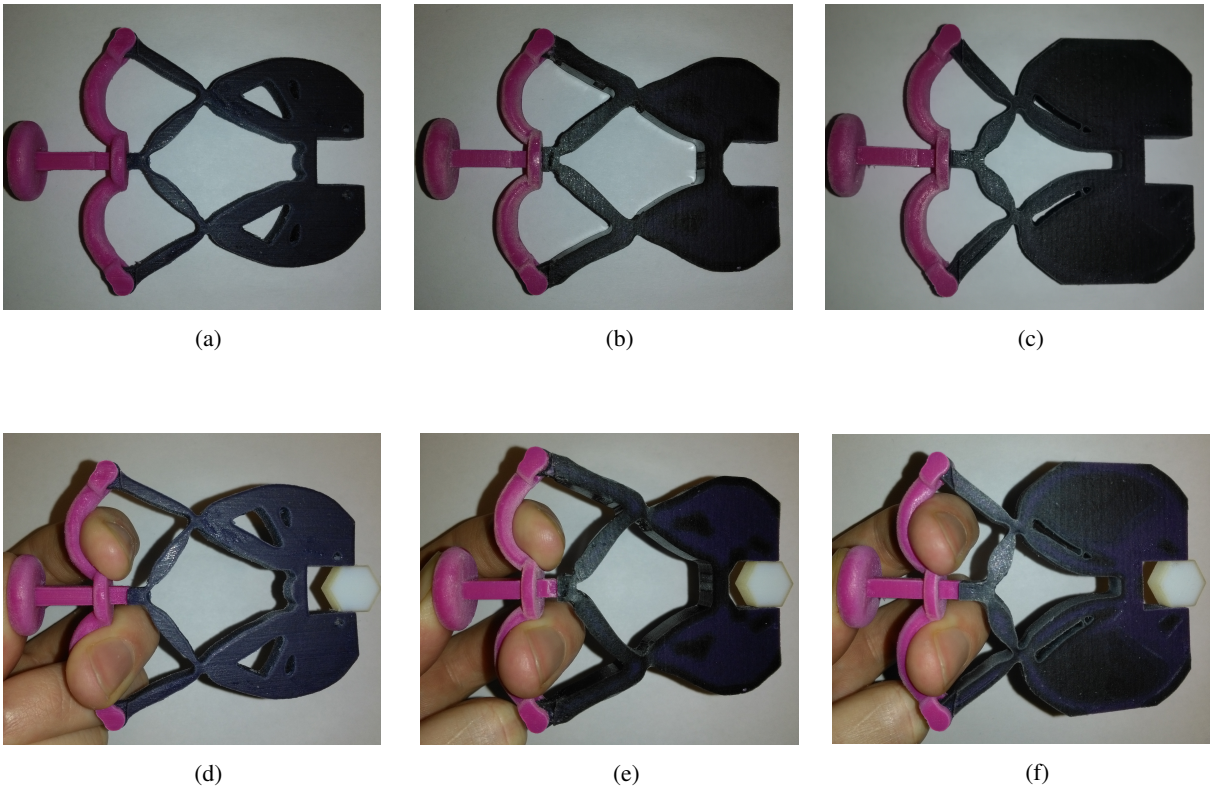

(a) (b) (c)

(d) (e) (f)

Figure 5.4: Large displacement gripper prototypes in undeformed (top) and deformed (bottom) configurations where (a) and (d) is the homogeneous mechanism, (b) and (e) is the volume-constrained FGM mechanism, and (c) and (f) is the modulus-constrained FGM mechanism.

5.1.2 Case b: Inverter problem

The inverter problem is solved for a unit input displacement (1 mm) and a larger displacement equal to 10% of the design domain length (6 mm). Similarly to the gripper problem, the analysis is first conducted on the homogeneous mechanism to obtain the value C_{min}. All inverter results are presented with a resource constraint, $\bar{M}$ of 0.3. The design problem is detailed in Figure 5.1b and has an objective function as to maximize geometric advantage. Material properties (found experimentally, refer to Appendix A) are the same for the inverter and gripper designs – Poisson's ratio of 0.4, homogeneous mechanisms are modeled with a Young's modulus of 11 MPa, and FGM mechanisms with a Young's modulus optimally varied between 0.14 MPa and 11 MPa based on location within the mechanism. Figures 5.5 and 5.6 show results for 1 mm and 6 mm input displacements respectively. Table 5.2 compares the geometric advantage and maximum von Mises stress for all 6 inverter designs.

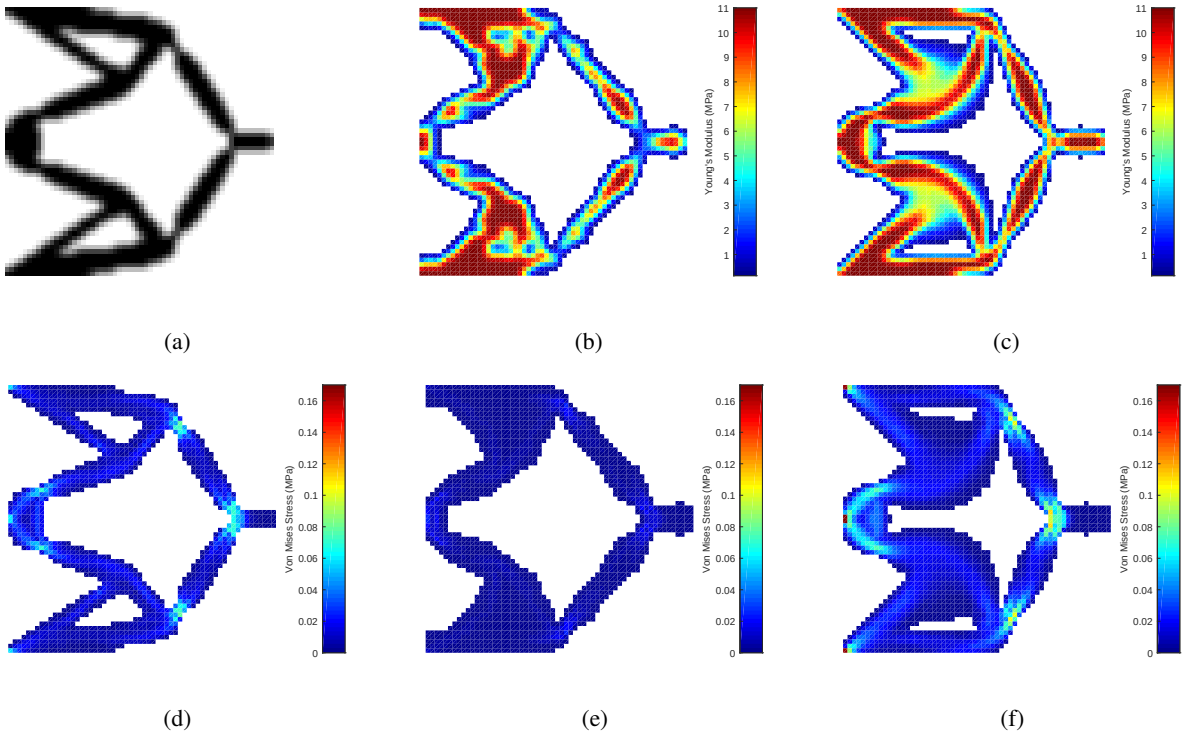

(a) (b) (c)

(d) (e) (f)

Figure 5.5: Inverter results for 1 mm input displacement. Converged topologies are shown on top – (a) homogeneous design, (b) FGM design with a volume constraint, (c) FGM design with a Young's modulus constraint. Von Mises stress distributions are shown on bottom – (d) homogeneous design, (e) FGM design with a volume constraint, (f) FGM design with a Young's modulus constraint.

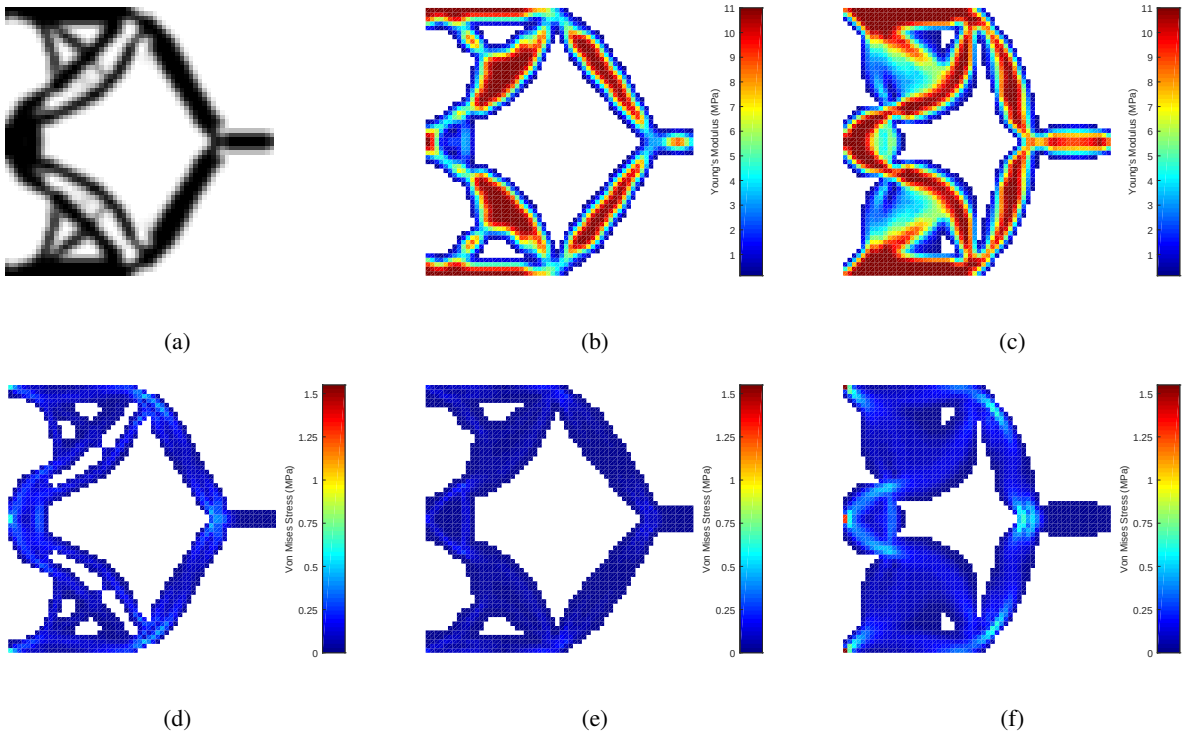

Figure 5.6: Inverter results for 6 mm input displacement. Converged topologies are shown on top – (a) homogeneous design, (b) FGM design with a volume constraint, (c) FGM design with a Young's modulus constraint. Von Mises stress distributions are shown on bottom – (d) homogeneous design, (e) FGM design with a volume constraint, (f) FGM design with a Young's modulus constraint.

			Void elements included		Void elements removed	
Material	***u_{in} (mm)***	***Constraint***	***Geo. Adv.***	***Max VM (MPa)***	***Geo. Adv.***	***Max VM (MPa)***
Homogeneous	1	-	1.33	0.0793	1.42	0.0257
FGM	1	Volume	1.02	0.0243	0.937	0.0107
FGM	1	Modulus	1.43	0.167	1.500	0.038
Homogeneous	6	-	0.898	0.597	0.997	0.144
FGM	6	Volume	0.832	0.252	0.760	0.0737
FGM	6	Modulus	0.952	1.53	1.12	0.307

Table 5.2: Comparison between inverter results with void element included and removed from the FEA mesh.

Compared to the homogeneous mechanisms, FGM mechanisms with volume constraints produce lower geometric advantages but also lower von Mises stresses – this observation is common to both gripper and inverter designs. When a modulus constraint is used, the geometric advantage is higher than the homogeneous mechanisms but so too are the von Mises stresses. There appears to be trade-off between increasing the geometric advantage of the mechanism and reducing stresses within the mechanism.

Comparing stress distributions and maximum von Mises stress in Table 5.2 it is very easy to see that the stresses

in the FGM mechanisms with a volume constraint are much lower than the other designs, and stress concentrations seem to have been eliminated. Homogeneous and modulus-constrained designs experience stress concentrations at the input location, boundary conditions, and compliant joints. Implementing FGMs with a modulus constraint seems to have no beneficial impact on the stress distributions in the inverter mechanisms.

New meshes were then created with all void elements removed from the mesh. Mechanical analysis was conducted once more on the new meshes and the results are shown in Table 5.2. With void elements removed, we see a large drop in maximum von Mises stress throughout all the designs, as well as a change in geometric advantage. For homogeneous mechanisms and modulus-constrained FGM mechanisms the geometric advantage is increased, with the FGM mechanism still being more advantageous. However, similar to the gripper case, the volume-constrained FGM mechanisms performed worse when the elements were removed with geometric advantage decreasing.

It is also worth noting that the inverter designed for a 6 mm displacement with a modulus constraint experiences a stress higher than the maximum ultimate strength of 1.4 MPa measured in the tensile tests (refer to Appendix A). However, once void elements are removed the maximum von Mises stress drops by 80% to well below the ultimate strength. This result inspired further work on stress-constrained FGM mechanisms to ensure materials do not fail (refer to Section 5.2).

Large displacement inverter mechanisms have also been prototyped and are shown in Figure 5.7. With geometric advantage mechanisms it is far easier to validate their performance experimentally. Geometric advantages obtained through testing these prototypes are presented and compared with computational results in Table 5.3. The differences in the geometric advantage of these prototype can be clearly seen in Figure 5.8 which shows the 3 mechanisms in their deformed configurations starting from the same datum.

(a) (b) (c)

(d) (e) (f)

Figure 5.7: Large displacement inverter prototypes in undeformed (top) and deformed (bottom) configurations where (a) and (d) is the homogeneous mechanism, (b) and (e) is the volume-constrained FGM mechanism, and (c) and (f) is the modulus-constrained FGM mechanism.

			Geometric Advantage		
Material	***u_{in} (mm)***	***Constraint***	**Void elements included**	**Void elements removed**	**Prototyped mechanisms**
Homogeneous	6	-	0.898	0.997	0.75
FGM	6	Volume	0.832	0.760	0.83
FGM	6	Modulus	0.952	1.12	1.33

Table 5.3: Comparison between inverter prototype results with computational results.

(a)

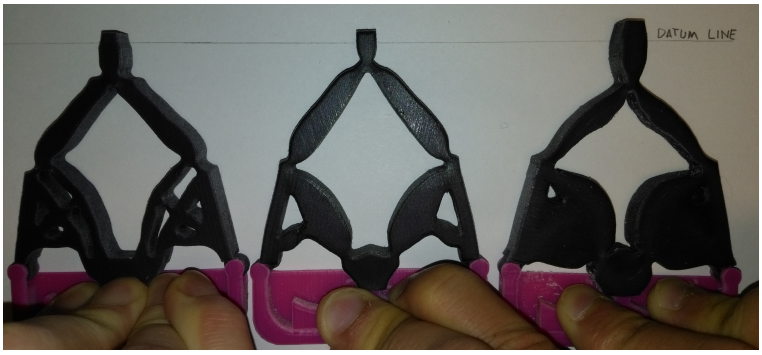

(b)

Figure 5.8: Comparison between output displacements in prototyped mechanisms. Homogeneous designs are shown on the left, FGM volume-constrained designs in the center and FGM modulus constrained designs on the right. (a) Shows the neutral starting position while (b) shows the extended position.

From the results in Table 5.3 we see that the FGM modulus-constrained inverter outperforms the other two mechanisms which is in keeping with the computational results. This result can be clearly seen in Figure 5.8. However we also see that the FGM volume-constrained design performs better than the homogeneous design which was not reflected in the computational results. There is significant error between experimental and computational results of up to 28% with void elements included and up to 33% with void elements removed. This then suggests that removing the elements does not create more accurate computational results with respect to geometric advantage. Further experimental analysis would be required to validate the stress distribution results. The FGM volume-constrained analysis with void elements included produced a result within 0.15% of the experimental result showing that this analysis can be accurate, however, further steps are required to ensure good accuracy. A major source of error comes with interpolating results in Figure 5.6 from a discrete finite element mesh design to a smooth material boundary. This interpolation was done by eye which holds a large margin for error and it is suggested that more accurate interpolation methods be explored for future work. One method to reduce this error is to use a finer mesh, however, this is not always possible with nonlinear analysis as computational costs become a major factor (as was the case here).

5.2 Design of Metallic Compliant Mechanisms

Metallic design problems are solved using linear FEA. For this analysis to be accurate we must ensure that the material does not yield. To do this we implement stress constraints. Design problems will be solved with homogeneous materials and FGM's. As the local material properties vary in the FGM structure, the structure will yield at different stresses depending on the yield stress of the local material. For the FGM case we use relationships between local yield stress, σ_y, and local Young's modulus, E_e. We use polynomial curve fits to produce a smooth, continuous, and differentiable E_e-σ_y relationship. For this work we will study two different FGM relationships. The FGMs will range from the most compliant to stiffest material in the following manner: Case (a) lead-copper-iron, and Case (b) lead-titanium-platinum-iron. All material properties were obtained from the online database MatWeb [80] and shown in Table 5.4. The two yield stress relationships are shown in Figure 5.9.

	Material	***Young's Modulus (GPa)***	***Yield Strength (MPa)***
Case (a)	Lead	14	18
	Copper	110	33
	Iron	200	50
Case (b)	Lead	14	18
	Titanium	116	140
	Platinum	171	125
	Iron	200	50

Table 5.4: Material properties used in analysis.

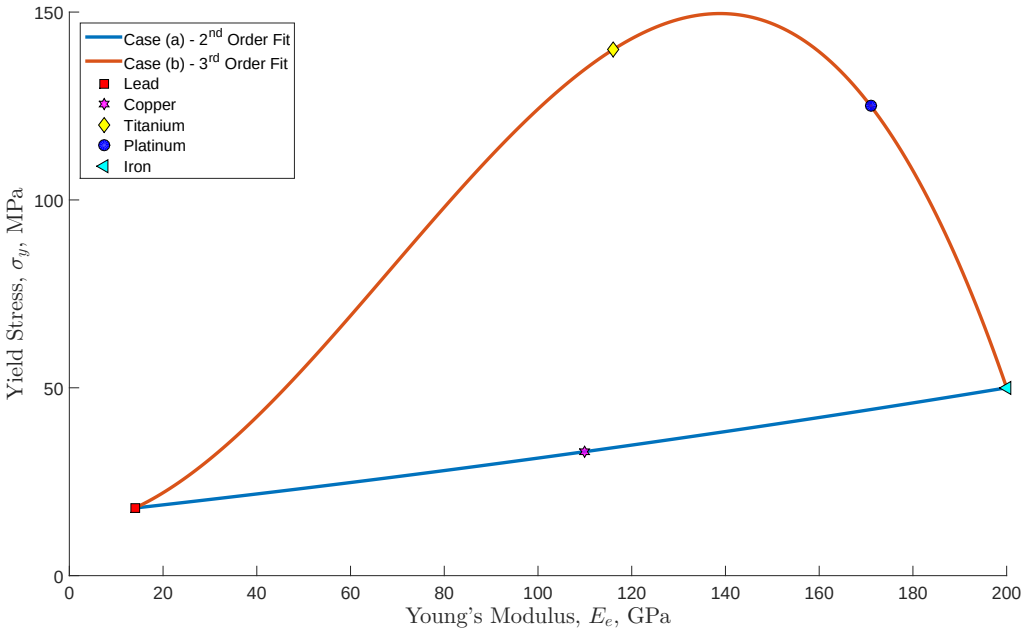

Figure 5.9: Yield stress-Young's modulus relationships for all four cases

5.2.1 Gripper problem

This section will present and compare homogeneous and FGM designs with and without constraints on maximum stress. To study the effects of stress constraints we seek to solve another gripper problem. The design problem is defined similarly to the previous gripper problem with an objective function to maximize mechanical advantage. The design domain is shown in Figure 5.10 and the design problem is defined in Eqn. 5.2.

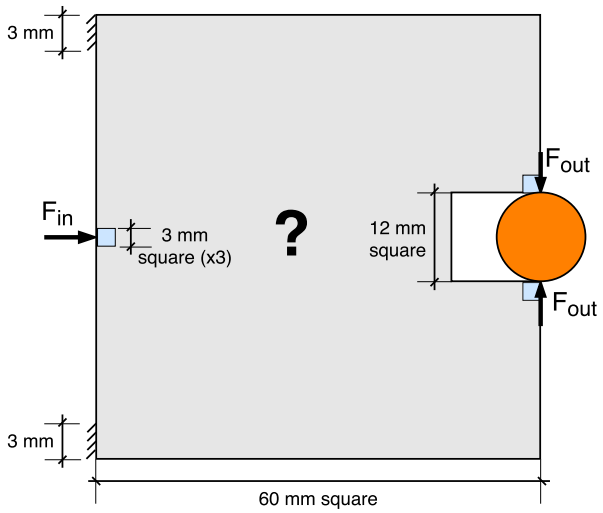

Figure 5.10: Stress constrained metallic gripper design domain with regions highlighted in blue that are exempt from the stress constraint.

$$
\begin{aligned}
\min_{x} \quad &: \quad g(\mathbf{u}(\boldsymbol{x}),\mathbf{f}(\boldsymbol{x}),\boldsymbol{x}) = \frac{F_{out}}{F_{in}} \\
\text{subject to} \quad &: \quad \int_{\Omega} \frac{M(\boldsymbol{x})}{M_0} d\Omega - \bar{M} \leq 0 \\
&: \quad C - C_{max} \leq 0 \\
&: \quad \left[\sum_{e=1}^{N_e} \left(x_e \eta \frac{\sigma_{VM}}{\sigma_y} \right)^{\zeta} \right]^{\frac{1}{\zeta}} - (1+\varepsilon) \leq 0 \qquad \text{for homogeneous design} \\
&\qquad \left[\sum_{e=1}^{N_e} \left(x_{0,e} \eta \frac{\sigma_{VM}}{\sigma_{y,E_e}} \right)^{\zeta} \right]^{\frac{1}{\zeta}} - 1 \leq 0 \qquad \text{for FGM design} \\
&: \quad \mathbf{0} < \boldsymbol{x}_{min} \leq \boldsymbol{x} \leq \mathbf{1}
\end{aligned}
\tag{5.2}
$$

The gripper results presented in Figures 5.2 and 5.3 show that the maximum von Mises stress occurs at the grippers inputs and outputs, however this is not the point of failure. The von Mises stress may be highest in these regions but a downfall of the von Mises yield criterion is its inability to determine whether an element is in compression or tension. Generally, materials fail exclusively in tension or shear as the yield strength in tension and shear is lower than in compression (refer to Section 3.3). Tensile yield strength is used in calculations as there is more material data available in tension. The gripper's input and output locations are examples of regions which experience high compression and therefore the von Mises stress may indicate yielding when it does not yield at these locations. This flaw in the von Mises yield criterion will cause the stress constraint to be satisfied prematurely in the optimization. To handle this the stress constraint is not enforced in the regions surrounding input and output locations. These regions are highlighted

as blue squares in Figure 5.10.

To demonstrate the behavior of gripper designs in failure we look to solve the homogeneous polymeric gripper design problem described in Figure 5.1 and Eqn. 5.1 with a higher input displacement of 10 mm to ensure the mechanism will fail. The topology and stress distribution of this problem is shown in Figure 5.11. The resource constraint, $\bar{M}$, is 0.3 and the minimum compliance is set to the value of compliance at the initial condition where each element density is equal to $\bar{M}$. The material has a Young's modulus is 11 MPa and Poisson ratio of 0.4 in keeping with results presented in Appendix A.

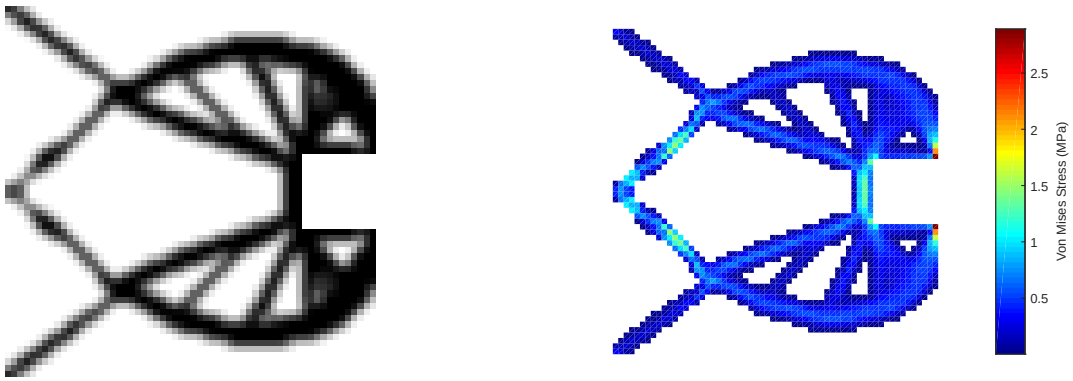

(a) (b)

Figure 5.11: Computational results for a polymeric gripper with 10 mm input displacement.

Once the design was prototyped it soon showed signs of failure as can be seen in Figure 5.12. From the stress distribution in Figure 5.11 we see that the maximum stress occurs at the output where as in Figure 5.12 we see that failure occurs at a compliant joint. Note also that the stress calculated in the region where failure occurs is close to the ultimate tensile stress of 1.4 MPa found in material testing (Appendix A).

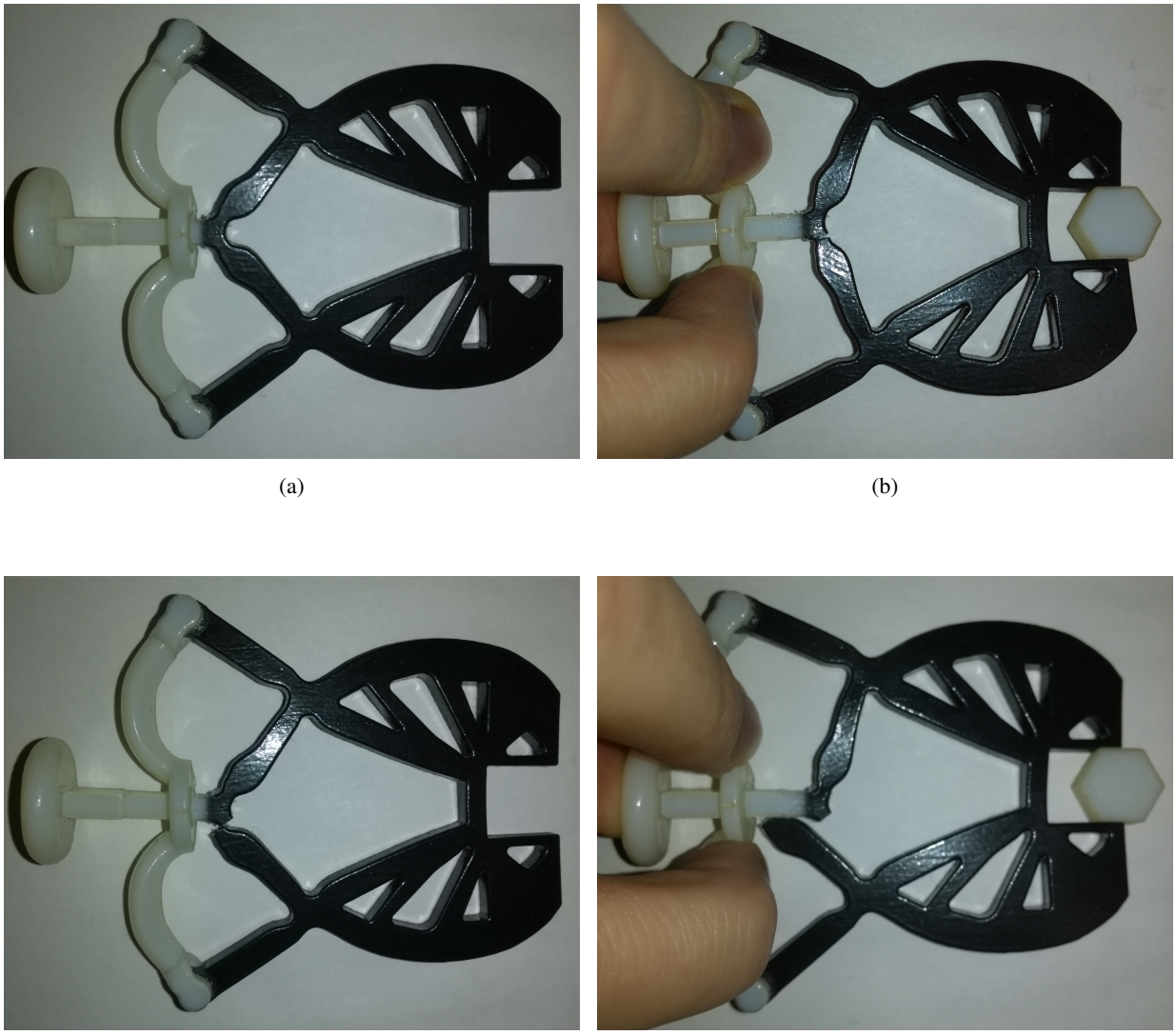

(a) (b)

(c) (d)

Figure 5.12: Prototyped mechanism in (a) undeformed configuration, (b) deformed configuration on the onset of failure, (c) and (d) after complete failure.

Homogeneous designs were modeled as the stiffest material, iron, which has a Young's modulus of 200 GPa and a yield strength of 50 MPa. Poisson's rtatio is assumed to be equal and constant for all mechanisms, and is taken to be 0.35, which is calculated as the average Poisson ratio of all materials used. All mechanisms have an input force of 50 N. Figure 5.13 shows homogeneous designs with and without stress constraints.

(a)

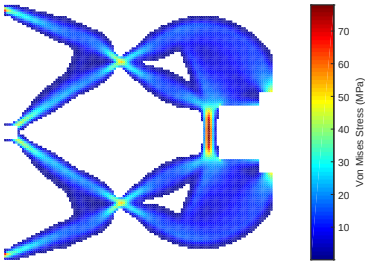

(b)

(c)

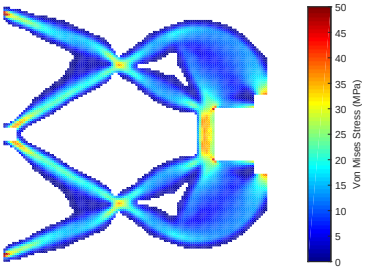

(d)

Figure 5.13: Homogeneous metallic designs without stress constraint (top) and with stress constraint (bottom), where (a) is the homogeneous topology without stress constraint, (b) the homogeneous stress distribution without stress constraint, (c) is the homogeneous topology with stress constraint, and (d) the homogeneous stress distribution with stress constraint.

By comparing the designs in 5.13 we can see that the stress constraint has altered the topology to reduce stresses in the structure. Maximum stress occurs at the back of the gripper's jaws. From Figure 5.13c we see the member in this region has been made thicker to redistribute and lower stresses (can also be seen in Figure 5.13d). Joints throughout the mechanism have too been made thicker in an effort to reduce stress.

FGM designs are produced with two different σ_y-E relationships, case (a) and case (b), as seen from Figure 5.9. Figures 5.14 and 5.15 shows volume- and modulus-constrained mechanisms respectively, with no stress constraint, case (a) and case (b). A comparison between mechanical advantages for all metallic mechanisms is shown in Table 5.5.

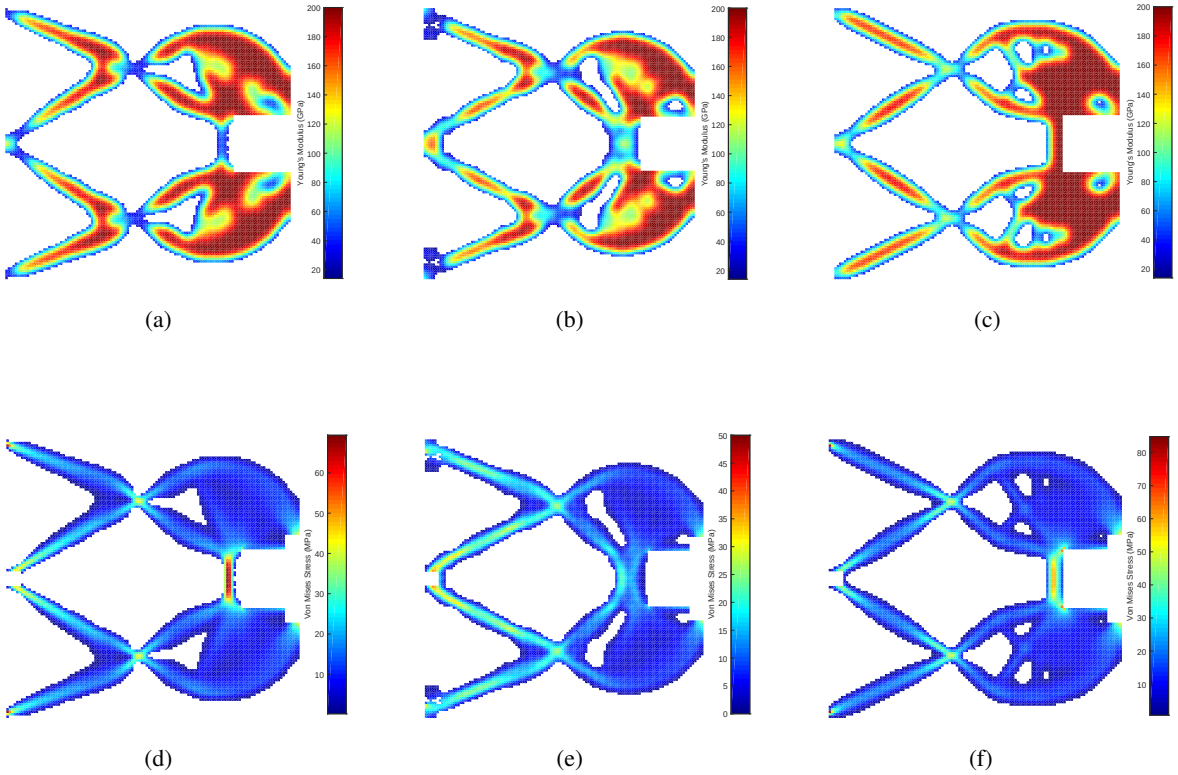

(a) (b) (c)

(d) (e) (f)

Figure 5.14: Volume constrained metallic gripper topologies (top) and stress distributions (bottom). (a) No stress constraint topology, (b) case a topology, (c) case b topology, (d) no stress constraint stress distribution, (e) case a stress distribution, (f) case b stress distribution.

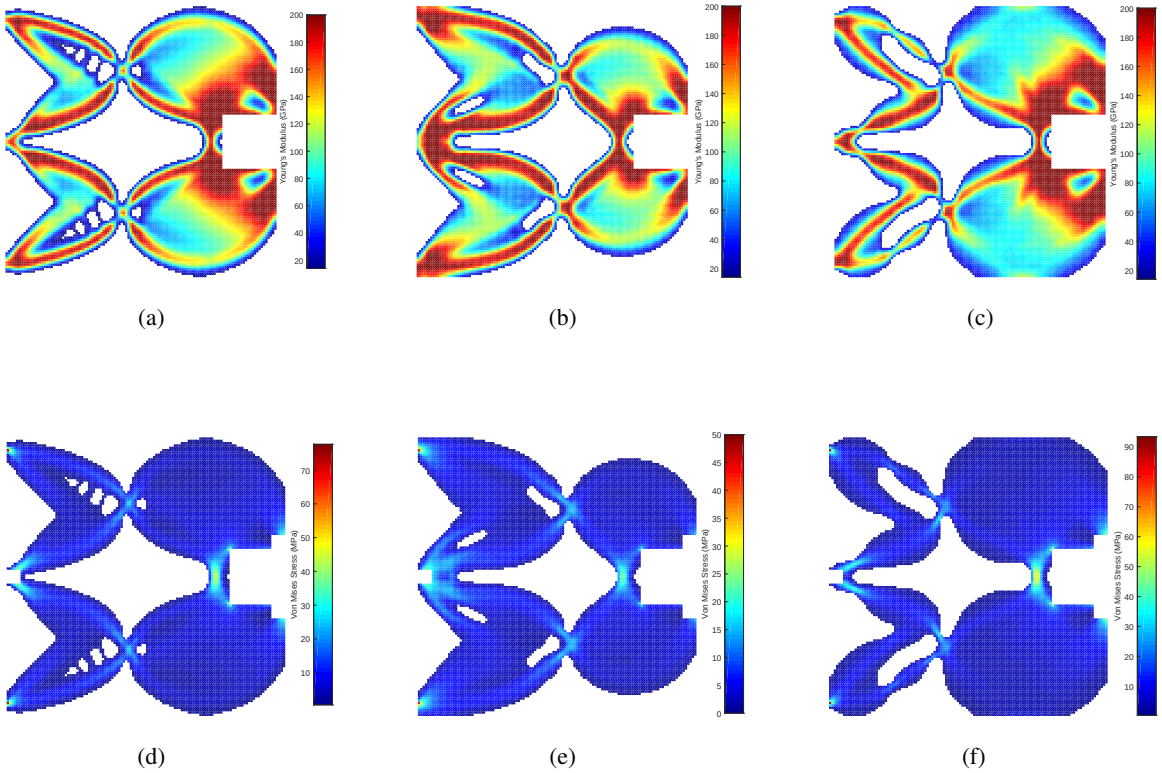

(a) (b) (c)

(d) (e) (f)

Figure 5.15: Modulus constrained metallic gripper topologies (top) and stress distributions (bottom). (a) No stress constraint topology, (b) case a topology, (c) case b topology, (d) no stress constraint stress distribution, (e) case a stress distribution, (f) case b stress distribution.

Homogeneous			***Functionally Graded***		
No Stress Constraint	***Stress Constraint***		***No Stress Constraint***	***Case (a)***	***Case (b)***
1.46	1.44	***Volume-Constained***	1.27	0.78	1.40
		Modulus-Constrained	1.14	0.41	1.03

Table 5.5: Comparison between mechanical advantage results for metallic grippers.

Figure 5.14 shows us that the maximum stress occurs at the back of the gripper's jaws for volume-constrained FGM mechanisms. The same results was observed for homogeneous designs. Case (a), like the homogeneous designs, has created a thicker member at the back of the gripper's jaws and thicker joints throughout the mechanism in order to reduce stresses. Case (b) includes materials with lower stiffness but higher yield strength. These more compliant materials can then be used in high stress areas to ensure the design does not fail. As a result, case (b) design still incorporates thinner members and joints throughout the mechanism.

Modulus constrained results are shown in Figure 5.15 and, in general, the designs experience lower stresses

throughout the structure compared to other two design methods. Highest stresses are experienced at the fixed points in these designs and so thicker members are used in these regions for case (a) and more compliant (higher yield strength) materials for case (b). In case (a) the majority of the material is distributed on the input side of the mechanism in order to satisfy the stress constraint. This has a knock-on effect of lowering the mechanical advantage capabilities as reflected in Table 5.5.

A comparison between mechanical advantage is presented in Table 5.5. One significant result is that homogeneous mechanisms perform better than FGM designs, which contradicts the previous results found for polymeric designs. The major differences between polymeric and metallic materials is that metals have much higher stiffness (difference of magnitude 10^4) and a much lower displacement (difference of magnitude 10^2). One major advantage of incorporating compliant materials comes with their ability to achieve larger deformation which can potentially lead to more efficient mechanisms. As metallic mechanisms experience minimal deformation this advantage is lost. Designs from case (b) perform better than designs from case (a). This result is expected as the σ_y-E relationship in case (b) is tailored to allow more compliant materials at no cost to the stress constraint. It is generally expected that the addition of constraints will lead to less efficient designs as they are constraining the design space. This holds true when stress constraints are introduced for most designs, however, the volume-constrained case (b) design performs better than the design without stress constraints. As the converged design in case (b) is possible in the design space when no stress constraint is used, we can conclude that the volume-constrained design without stress constraints is a local minimum (refer to section 2.3.4).

Chapter 6

Conclusions

We presented the hypothesis that implementing functionally graded materials in the design of compliant mechanisms will produce more efficient designs through increasing mechanical/geometric advantage and improving stress distributions. In order to conduct this study this thesis has introduced novel methods for modeling local element material properties in FGM structures. We have also introduced a novel method for stress-based topology optimization of FGM structures. The theory and methods presented in the opening chapters of this thesis have been implemented to produce compliant mechanism designs using polymeric and metallic materials.

It has been found from the polymeric gripper results that with small input displacements, incorporating FGMs into compliant mechanism design with a modulus constraint both improves mechanical advantage and stress distributions, which affirms our hypothesis for the mechanical advantage problem. However this is dependent on the resource constraint as the volume-constrained designs failed to produce either higher mechanical advantages or improved stress distributions. For higher input displacements, we found that homogeneous designs produced a higher mechanical advantage, but also higher stresses throughout the mechanism. For polymeric inverters, or geometric advantage problems, we notice a trade-off between geometric advantage and stress distributions with the resource constraint. By using a volume constraint, the stresses throughout the mechanism are significantly reduced, and stress concentrations are eliminated, but with the negative effect of reducing geometric advantage. Conversely, when a modulus constraint is used, the geometric advantage of the mechanism increased compared to a homogeneous design, but with the negative effect of increasing stresses throughout the mechanism. Results also suggest that the presence of void elements in converged designs has a significant effect on results. One case saw a material failing under high stresses, but once void elements were removed these stresses dropped by 80%, which is significantly below the ultimate strength of the material. We therefore conclude that implementing FGMs in compliant mechanism design has a positive impact on the mechanism's structural performance, however the value of this impact is dictated by the design problem and design methods.

Polymeric inverter results were prototyped and tested experimentally to validate computational results. It was

found that both volume- and modulus-constrained FGM mechanisms performed better than the homogeneous mechanism, which was not shown in computational results. Consistency between experimental and computational results was achieved in one (out of three), and removing void elements from the design domain has no beneficial effect on the achieving this consistency. This shows that good consistency can be achieved, however further steps should be taken in order to ensure consistency. One major source of error between computational and experimental results is caused by coarseness of the mesh as some interpolation is required. Here, interpolation of the material boundary was performed manually, which has a large margin for error.

A formulation for modeling stress constraints in functionally graded structures has been successfully implemented. This formulation takes yield strength to be a function of local Young's modulus. Relationships between yield strength and Young's modulus have been studied and presented. Results for metallic designs are inconsistent with polymeric design results, as the FGM mechanisms were less efficient than the homogeneous mechanisms. One source for this could be that these mechanisms experience very little displacement ($<$0.1 mm), whereas a major advantage of functionally graded materials is that they incorporate more compliant materials that can achieve displacement easily at low stress. These compliant materials are also less efficient at transmitting loads as they are easily deformed.

Appendices

Appendix A

Materials Testing

To conduct the mechanical analysis described in Chapter 3 we require two independent material properties, namely the Young's modulus, E, and the Poisson's ratio, ν. These material properties are used to calculate the Lamé constants which in turn was used in the analysis. The material properties used in the mechanical analysis were based on materials available for prototyping. These material properties were achieved through simple tensile tests in accordance with ASTM standard D638 [81].

Prototypes have been created using a Polyjet 3D printer by Stratasys (Objet260 Connex3). Two Stratasys materials are modeled, TangoBlack+ and a material blend of TangoBlack+, RGD531 and RGD515 (digital material code FLX95595). Both materials experience hyperelastic behavior, however material 1 (TangoBlack+) is a highly flexible, compliant material, whereas material 2 (blend FLX95595) is a much stiffer material. The homogeneous models are based on material 2 only (stiffer material), whereas the FGM models are able to use any mixing ratio of the two materials. Because both materials are non-rigid, so flat dog-bone specimens were produced based on the type 4 specimen in [81].

A.1 Young's Modulus

The universal testing machine (UTM) recorded load data, but because the materials are so flexible (especially material 1), the specimens could not be fitted with any available extensometers as the weight of the instrument alone deforms the specimen. Relying on the crosshead speed for extension, and subsequently strain data, is too unreliable as there is too much deformation outside the specimen's gauge length. Instead the entire experiment was recorded, giving the view on the right in Figure A.1. The camera started to record simultaneously with the UTM. The elongation of the specimen can then be determined by reviewing the recordings of the experiment. Notice how the gauge length is clearly marked on the test specimen, this gauge length is measured prior to testing. At time zero in the video recording, the gauge length of the specimen can be measured on screen, and a linear mapping can be produced between

the real gauge length (prior to testing) and the on-screen gauge length. This mapping can then be used to convert the onscreen deformed gauge length at specific times in the test video to the real deformed gauge length. Based on this data, elongation and strain values at specific times can be achieved and linked to corresponding load values from the UTM data. A crosshead speed of 50 mm/min was used for both materials. The specimen and experimental set up is shown in Figure A.1. It is also important to note that smooth grip jaws were used as knurled jaws could pierce and damage the soft specimen, producing stress concentrations and causing the specimen to fail outside of the gauge length.

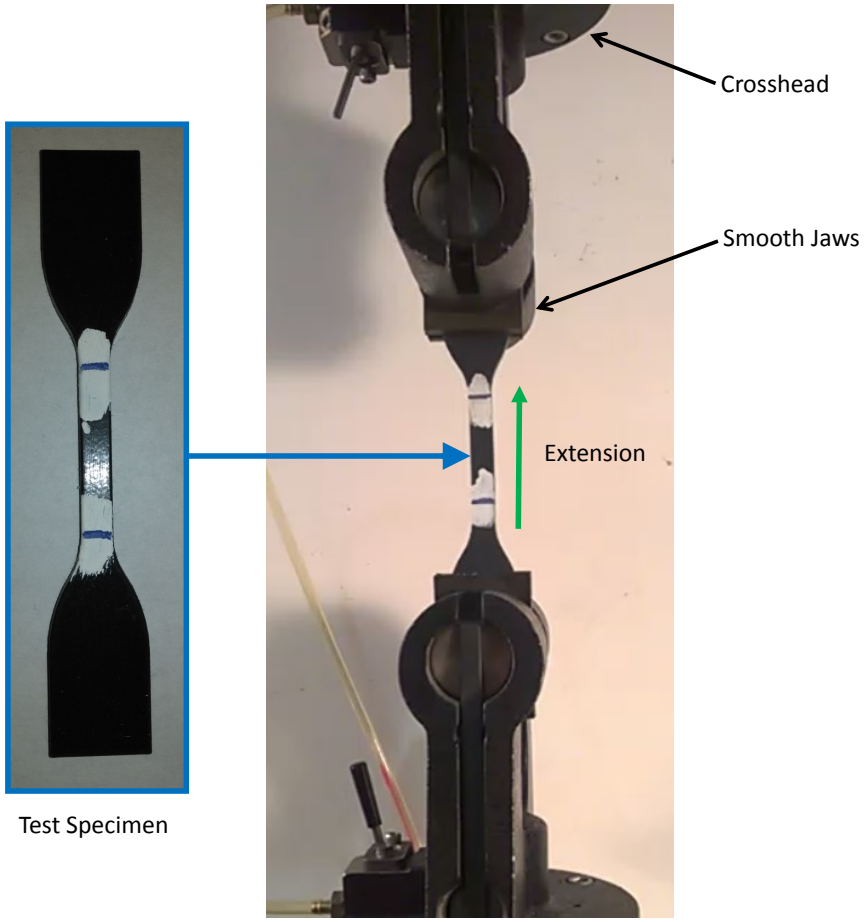

Figure A.1: Experimental setup is shown on the right and detail of the specimen on the left.

Stress-Strain relationships are then be produced and analyzed to find values for Young's modulus as described in [81]. Based on mean values of 6 samples, material 1 was found to have a Young's modulus of 0.14 MPa, and material 2, a Young's modulus of 11 MPa. Stress-Strain relationships for the 6 samples of each material are shown below. All samples were tested to failure.

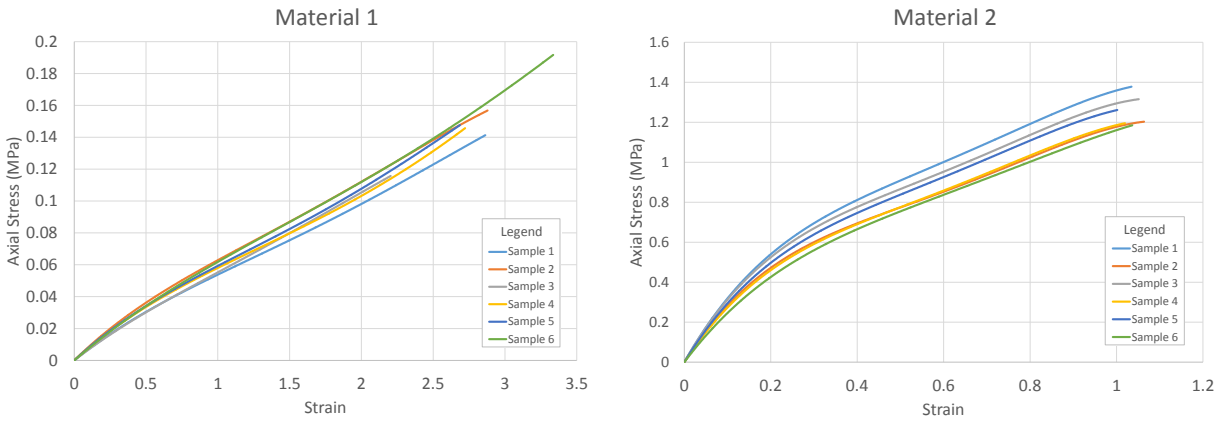

(a) (b)

Figure A.2: Test data for (a) material 1 and (b) material 2.

A.2 Poisson's Ratio

The Poisson's ratio was found by mounting the specimen in the UTM as shown in Figure A.1 and extending in the axial direction in small incremental steps whilst remaining within the linear elastic region. At each increment the deformation in axial and transverse directions were recorded and used to calculate strains in the axial, ε_z, and transverse directions, ε_x, ε_y. Poisson's ratio, by definition, is then calculated as

$$\nu = -\frac{d\varepsilon_x}{d\varepsilon_z} = -\frac{d\varepsilon_y}{d\varepsilon_z} \tag{A.1}$$

where ε_z is axial strain, and ε_x and ε_y are the transverse strains. Poisson's ratio was taken to be an average of all recorded measurements. It was later found that material 1 is too compliant to obtain accurate readings using vernier calipers as it is too easy for the calipers to deform the specimen. Instead, it was assumed that the Poisson's ratio of material 1 is equal to the Poisson's ratio of material 2. Based on mean values of 5 readings the Poisson's ratio of material 2 was found to be 0.4.

References

[1] Sigmund, O., "On the Design of Compliant Mechanisms Using Topology Optimization" Mechanics of Structures and Machines: An International Journal, vol. 25, no. 4, pp. 493-542, 1997.

[2] J. Buck, T Mc Mahon, D. Huot, "Space Station 3-D Printer Builds Ratchet Wrench To Complete First Phase Of Operations," 22 Dec. 2014. [Online]. Available: `https://www.nasa.gov/mission_pages/station/research/news/3Dratchet_wrench`. [Accessed 12/12/2016].

[3] T. J. Prater, Q. A. Bean, R. D. Beshears, T. D. Rolin, N. J. Werkheiser, E. A. Ordonez, R. M. Ryan, F. E. Ledbetter III, "Summary Report on Phase I Results from the 3D Printing in Zero G Technology Demonstration Mission, Volume I," NASA Technical Reports Server, Jul. 1st 2016.

[4] OpenStax, "Anatomy & Physiology", OpenStax, 2013.

[5] A. Marin, A. A. Fuentes, "Human Bone: Functionally Graded Material Structures with Complex Geometry and Loading," Department of Mechanical Engineering, University of Texas-Pan American.

[6] D. Wolf, S. Yip, "Material Interfaces: Atomic-level Structure and Properties," Netherlands: Springer, 1993.

[7] Y. Miyamoto, W. A. Kaysser, B. H. Rabin, A. Kawasaki, R. G. Ford, "Functionally Graded Materials: Design, Processing and Applications," Springer, 1999.

[8] C. Alonso, "Topology synthesis of multi-material complaint mechanisms with Sequential Element Rejection and Admission," Finite Elements in Analysis and Design, vol. 85, pp. 11-19, 2014.

[9] L. Yin, G. K. Ananthasuresh, "Topology optimization of compliant mechanisms with multiple materials using a peak function material interpolation scheme," Structural and Multidisciplinary Optimization, vol. 23, no. 1, pp. 49-62, 2003.

[10] M. P. Bendsøe, O. Sigmund, "Material interpolation schemes in topology optimization," Archive of Applied Mathematics, vol. 69, pp. 635-654, 1999.

[11] O. Sigmund, "Design of multiphysics actuators using topology optimization Part II: Two-material structures," Computer Methods in Applied Mechanics, vol. 190, no. 49-50, pp. 6605-6627, 2001.

[12] O. Sigmund, S. Torquato, "Design of materials with extreme thermal expansion using a three-phase topology optimization method," Journal of the Mechanics and physics of Solids, vol. 45, no. 6, pp. 1037-1067, 1997.

[13] J. Stegmann, E. Lund, "Discrete material optimization of general shell structures," International Journal for Numerical Methods in Engineering, vol. 62, no. 14, pp. 2009-2027, 2005.

[14] A. Gaynor, N. A. Meisel, C. B. Williams, J. K. Guest, "Multiple-Material Topology Optimization of Compliant Mechanisms Created via Polyjet Three-Dimensional Printing," Journal of Manufacturing Science and Engineering, vol. 136(6), 2014.

[15] R. C. Carbonari, G. H. Paulino, E. C. N. Silva, "Integral Piezoactuator with Optimum Placement of Functionally Graded Material - A Topology Optimization Paradigm," Journal of Intelligent Material Systems and Structures, vol. 21, no. 16, pp. 1653-1668, 2010.

[16] R. C. Carbonari, E. C. N. Silva, G. H. Paulino, "Multi-actuated functionally graded piezoelectric micro-tools design: A multiphysics topology optimization approach," International Journal for Numerical Methods in Engineering, vol. 77, no. 3, pp. 301-336, 2009.

[17] L. Yin, G. K. Ananthasuresh, "A novel topology design scheme for the multi-physics problems of electro-thermally actuated compliant micromechanisms," Sensors and Actuators A: Physical, Vols. 97-98, pp. 599-609, 2002.

[18] Q. Xia, M. Yu Wang, "Simultaneous optimization of the material properties and the topology of functionally graded structures," Computer-Aided Design, ACM Symposium on Solid and Physical Modeling and Applications, vol. 40, no. 6, pp. 660-675, 2008.

[19] F. V. Stump, E. C. N. Silva, G. H. Paulino, "Optimization of material distribution in functionally graded structures with stress constraints," Communications in Numerical Methods in Engineering, vol. 23, no. 6, pp. 535-551, 2007.

[20] A. G. M. Michell, "The limits of economy of material in frame-structures," Philosophical Magazine, Vol. 8, no. 47, pp. 589-597, 1904.

[21] G. I. N. Rozvany, "Grillages of maximum strength and maximum stiffness," International Journal of Mechanical Sciences, vol. 14, pp. 1217-1222, 1972.

[22] G. I. N. Rozvany, "Optimal load transmission by flexure," Methods Applied Mechanics and Engineering, vol. 1, pp. 253-263, 1972.

[23] U. Kirsch, "Optimal design of trusses by approximate compatibility," Computers and Structures, vol. 12, pp. 93-98, 1979.

[24] R.T. Haftka, R.V. Gandhi, "Structural shape optimization," Computer Methods in Applied Mechanics and Engineering, vol. 57, pp. 91-106, 1986.

[25] M.P. Bendsøe, N. Kikuchi, "Generating optimal topologies in structural design using a homogenization method," Computer Methods in Applied Mechanics and Engineering, vol. 71, pp. 197-224, 1988.

[26] M. P. Bendsøe, O. Sigmund, "Topology Optimization: Theory, Methods and Applications," Berlin Heidelberg: Springer-Verlag, 2004.

[27] O. Sigmund, "A 99 Line Topology Optimization Code Written in Matlab," Structural Multidisciplinary Optimization, vol. 21, no. 2, pp. 120-127, 2001.

[28] E. Andreassen, A. Clausen, M. Schevenels, B.S. Lazarov, O. Sigmund, "Efficient Topology Optimization in MATLAB Using 88 Lines of Code," Structural Multidisciplinary Optimization, vol. 43, no. 1, pp. 1-16, 2010.

[29] M. P. Bendsøe, "Optimal shape design as a material distribution problem," Structural optimization, vol. 1, no. 4, pp. 193-202, 1989.

[30] M. P. Bendsøe, O. Sigmund, "Material Interpolation Scheme in Topology Optimization," Archive of Applied Mechanics, Vol. 69, no. 9, pp. 635-654, 1999.

[31] M. Y. Wang, X. Wang, D. Guo, "A Level Set Method for Structural Optimization," Computer Methods in Applied Mechanics and Engineering, Vol. 192, no. 1-2, pp. 227-246, 2003.

[32] E. Haber, "A multilevel, level-set method for optimizing eigenvalues in shape design problems," Journal of Computational Physics, Vol. 198, no. 2, pp. 518-534, 2004.

[33] O. Sigmund, J. Petersson, "Numerical instabilities in topology optimization: A survey on procedures dealing with checkerboards, mesh-dependencies and local minima," Structural Optimization, vol. 16, pp. 68-75, 1998.

[34] C. S. Jog, R. B. Haber, "Stability of finite element models for distributed parameter optimization and topology design," Computer Methods in Applied Mechanics and Engineering, vol. 130, pp. 203-226, 1996.

[35] C. Talischi, G. H. Paulino, A. Pereira, I. F. M. Menezes, "Polygonal finite elements for topology optimization: A unifying paradigm," vol. 82, no. 6, pp. 671-698, 2010.

[36] H. Zhou, "Topology Optimization of Compliant Mechanisms Using Hybrid Discretization Model," Journel of Mechanical Design, vol. 132, no. 11, 2010.

[37] M.P. Bendsøe, N. Kikuchi, N. Diaz, "Topology and generalized layout optimization of elastic structures," Topology Design of Structures, Springer Netherlands, pp 159-205, 1993.

[38] K. Svanberg, M. Werme, "A hierarchical neighbourhood search method for topology optimization," Structural and Multidisciplinary Optimization, vol. 29, pp. 325-340, 2005.

[39] T. E. Bruns, D. A. Totorelli, "Topology optimization of non-linear structures and compliant mechanisms," Computer Methods in Applied Mechanics and Engineering, vol. 190, no. 26-27, pp. 3443-3459, 2001.

[40] B. Bourdin, "Filters in topology optimization," International Journal for Numerical Methods in Engineering, vol. 50, pp. 2143-2158, 2001.

[41] G. Allaire, G.A. Francfort, "A numerical algorithm for topology and shape optimization," In: M.P. Bendsøe, C.A. Mota Soares, "Topology design of structures," pp. 239-248, Dordrecht: Kluwer, 1993.

[42] G. Allaire, R.V. Kohn, "Topology optimization and optimal shape design using homogenisation," In: M.P. Bendsøe C.A. Mota Soares, "Topology design of structures," pp. 207-218, Dordrecht: Kluwer, 1993.

[43] R.B. Haber, C. Jog, M.P. Bendsøe, "A new approach to variable-topology shape design using a constraint on the perimeter," Structural and Multidisciplinary Optimization, vol. 11, pp. 1-12, 1996.

[44] J. Petersson, O. Sigmund, "Slope Constrained Topology Optimization," International journal for Numerical Methods in Engineering, vol 41, pp. 1417-1434, 1998.

[45] K. A. James, H. Waisman, "Layout design of a bi-stable cardiovascular stent using topology optimization," Computer Methods in Applied Mechanics and Engineering, vol. 305, pp. 869-890, 2016.

[46] J. M. Guedes, J.E. Taylor, "On the prediction of material properties and topology for optimal continuum structures," Structural and Multidisciplinary Optimization, vol. 14, pp. 183-192, 1997.

[47] S. Grihon, L. Krog, K. Hertel, "A380 Weight Savings Using Numerical Structural Optimization," in proceedings of 20^{th} AAAF Colloquium Material for Aerospace Applications, Paris, 2004.

[48] M. Zhou, R. Fleury, S. Patten, N. Stannard, D. Mylett, S. Gardner, "Topology Optimization –Practical Aspects for Industrial Applications," in proceedings of the 9th World Congress on Structural and Multidisciplinary Optimization, Shizuoka, Japan, 2011.

[49] T. Zegard, G. H. Paulino, "Bridging topology optimization and additive manufacturing," Structural and Multidisciplinary Optimization, vol. 53, no. 1, pp. 175-192, 2016.

[50] D. Brackett, I. Ashcroft, R. Hague, "Topology optimization for additive manufacturing," in proceedings of the 22nd Annual International Solid Freeform Fabrication Symposium, Austin, TX, 2011.

[51] L. Krog, A. Tucker, M. Kamp, R. Boyd, "Topology Optimization of Aircraft Wing Box Ribs," in proceedings of the Altair Technology Conference 2004, vol. 6, Altair Engineering, Troy, MI, 2004.

[52] D. Xiao, H. Zhang, X. Liu, T. He, Y. Shan, "Novel steel wheel design based on multi-objective topology optimization," Journal of Mechanical Science and Technology, vol. 28, no. 3, pp. 1007-1016, 2014.

[53] BGN S. Prasad, M. A. Kumar, "Topology Optimization of Alloy Wheel," in proceedings of 2013 India Altair Technology Conference, Ghorpadi Pune, 2013.

[54] T. Belytschko, W. K. Liu, B. Moran, K. Elkhodary, "Nonlinear Finite Elements for Continua and Structures," Wiley, Chichester, West Sussex, UK, 2002.

[55] C. B. W. Pedersen, T. Buhl, O. Sigmund, "Topology synthesis of large-displacement complaint mechanisms," Numerical Methods in Engineering, vol. 50, no. 12, pp. 2683-2705, 2001.

[56] H. C. Gea, J. Luo, "Topology optimization of structures with geometrical nonlinearities," Computers & Structures, vol. 79, no. 20-21, pp. 1977-1985, 2001.

[57] N. H. Kim, "Introduction to Nonlinear Finite Element Analysis," New York: Springer US, 2015.

[58] P. Wriggers, "Nonlinear Finite Element Methods," Springer, Berlin Heidelberg, 2008.

[59] A. S. Ramos Jr., G. H. Paulino, "Convex topology optimization for hyperelastic trusses based on the ground-structure approach," Structural and Multidisciplinary Optimization, vol. 51, no. 2, pp. 287-304, 2015.

[60] F. A. Gomes, T. A. Senne, "An algorithm for the topology optimization of geometically nonlinear structures," International Journal for Numerical Methods in Engineering, 2014.

[61] Y. Lou, M. Li, Z. Kang, "Topology optimization of hyperelastic structures with frictionless contact supports," International Journal of Solids and Structures, vol. 81, pp. 373-382, 2016.

[62] Y. Basar, D. Weichert, "Nonlinear Continuum Mechanics of Solids: Fundamental Mathematical and Physical Concepts," Springer-Verlag, Berlin Heidelberg, 2000.

[63] G. Marckmann and E. Verron, "Comparison of Hyperelastic Models for Rubber-Like Materials," Rubber Chemistry and Technology, vol. 79, no. 5, pp. 835-858, 2006.

[64] J. L. Batoz, G, Dhatt, "Incremental displacement algorithms for nonlinear problems," International Journal for Numerical Methods in Engineering, vol. 14, no. 8, pp. 1262-1267, 1979.

[65] M. Zhou, G. I. N. Rozvany, "The COG algorithm, Part II: Topological, geometrical and generalized shape optimization," Computer Methods in Applied Mechanics and Engineering, vol. 89, no. 1-3, pp. 309-336, 1991.

[66] P. Duysinx, M.P. Bendsøe, "Topology optimization of continuum structures with local stress constraints," International Journel for Numerical Methods in Engineering, vol. 43, no. 8, pp. 1453-1478, 1998.

[67] P. Duysinx, O. Sigmund, "New Developments in Handling Stress Constraints in Optimal Material Distribution," In proceedings of the 7^th AIAA/USAF/NASA/ISSMO symposium on multidisciplinary analysis and optimization, 1998.

[68] C. Le, J. Norato, T. Bruns, C. Ha, D. Tortorelli, "Stress-based topology optimization for continua," Structural and Multidisciplinary Optimization, vol 41, pp. 605-620, 2010.

[69] E. Lee, K.A. James, J.R.R.A. Martins, "Stress-Constrained Topology Optimization with Design Dependent Loading," Structural and Multidisciplinary Optimization, vol. 46, no. 5, pp. 647-661, 2012.

[70] R. von Mises, "Mechanik der Festen Körper im Plastisch Deformablen Zustand," Nachrichten von der Gesellschaft der Wissenschaften zu Göttingen, Mathematisch-Physikalische Klasse, Zeitschriftenband, pp. 582-592, 1913.

[71] G.I. Taylor, H. Quinney, "The Plastic Distortion of Metals," Philosophical Transactions of the Royal Society, vol. 230, pp. 323-362, 1931.

[72] H. Tresca, "Sur l'Ecoulement des Corps Solides Soumis a de Fortes Pressions," Comptes Rendus de l'Acadèmie des Sciences, vol. 59, pp. 754, 1864.

[73] R.G. Budynas, J.K. Nisbett, J.E. Shigley "Shigley's Mechanical Engineering Design," 8^th Edition, McGraw-Hill, 2008.

[74] G.C. RauchW, C. Leslie, "The extent and nature of the strength-differential effect in steels," Metallurgical and Materials Transactions, vol. 3, no. 2, pp. 377-389, 1972.

[75] D.C. Drucker, "Plasticity theory strength-differential (SD) phenomenon and volume expansion in metals and plastics," Metallurgical and Materials Transactions, vol. 4, no. 3, pp. 667-673, 1973.

[76] A.P. Singh, K.A. Padmanabhan, G.N. Pandey, G.M.D. Murty, S. Jha, "Strength differential effect in four commercial steels," Journal of Materials Science, vol. 35, no. 6, pp. 1379-1388, 2000.

[77] K. Svanberg, "The method of moving asymptotes — a new method for structural optimization," International Journal for Numerical Methods in Engineering, vol. 24, no. 2, pp. 359-373, 1987.

[78] W. Karush, "Minima of functions of several variables with inequalities as side constraints," Master's Thesis, University of Chicago, Chicago, IL, 1939.

[79] H. Kuhn, A. Tucker, "Nonlinear Programming," in Proceedings of 2nd Berkeley Symposium, Berkeley, CA, 1951.

[80] "MatWeb – Material Property Data," [Online]. Available: `https://www.matweb.com/index.aspx`. [Accessed 4/3/2017].

[81] "ASTM D638-14 Standard Test Method for Tensile Properties of Plastics," ASTM International, 2014.

[82] N. Coburn, P. G. Hodge, "Theory of Perfectly Plastic Solids," Mathematics Magezine, vol. 27, no. 4, pp. 231-232, 1954.

[83] G. A. Holzapfel, "Nonlinear Solid Mechanics: A Continuum Approach for Engineering Science," New York: John Wiley & Sons, 2000.

[84] C. Alonso, O. M. Querin, R. Ansola, "A Sequential Element Rejection and Admission (SERA) method for compliant mechanisms design," Structural and Multidisciplinary Optimization, Springer-Verlag, Berlin, 2013.

[85] G. Udupa, S. S. Rao, K. V. Gangadharan, "Functionally Graded Composite Materials: An Overview," Procedia Materials Science, Elsevier, vol. 5, pp. 1291-1299, 2014.

[86] A. Saxena, "Topology Design of Large Displacement Compliant Mechanisms with Multiple Materials and Multiple Output Ports," Structural Multidisciplinary Optimization, Spring-Verlag, 2005.

[87] S. R. M. Almeida, G. H. Paulino, E. C. N. Silva, "Layout and material gradation in topology optimization of functionally graded structures: a globallocal approach," Structural and Multidisciplinary Optimization, vol. 42, no. 6, pp. 855-868, 2010.

[88] N. Vermaak, G. Michailidis, G. Parry, R. Estevez, G. Allaire, Y. Brechet, "Material interface effects on topology optimization of multi-phase structures using a level set method," Structural and Multidisciplinary Optimization, vol. 50, no. 4, pp. 623-644, 2014.